

YRHI-98-13

Yale Relativistic Heavy Ion Group

Relativistic Heavy Ion Physics and the Relativistic Heavy Ion Collider

John W. Harris

*Physics Department, Yale University
New Haven CT 06250, U.S.A.*

Three lectures given at the Lake Louise Winter Institute on Quantum Chromodynamics, 15 - 21 February, 1998, Lake Louise, Alberta, Canada, to be published in World Scientific 1998.

RELATIVISTIC HEAVY ION PHYSICS AND THE RELATIVISTIC HEAVY ION COLLIDER

J. W. HARRIS

*Physics Department, Yale University
New Haven CT 06250, U.S.A.*

1 Introduction

The primary motivation for studying relativistic heavy ion collisions is to gain an understanding of the equation of state of nuclear, hadronic and partonic matter, commonly referred to as nuclear matter. This endeavor is of cross-disciplinary interest to nuclear physics, astrophysics, cosmology and particle physics. Displayed in Fig.1 is a schematic phase diagram of nuclear matter. The behavior of nuclear matter as a function of temperature and density (or pressure), shown in Fig.1, is governed by its equation of state. Conventional nuclear physics is concerned primarily with the lower left portion of the diagram at low temperatures and near normal nuclear matter density. Here normal nuclei exist and at low excitation a liquid-gas phase transition is expected to occur. This is the focus of experimental studies using low energy heavy ions. At somewhat higher excitation, nucleons are excited into baryonic resonance states, along with accompanying particle production and hadronic resonance formation. In heavy ion collisions, such excitation is expected to create hadronic resonance matter. This region is presently accessible in heavy ion studies at the AGS accelerator facility at Brookhaven National Laboratory and at the SPS accelerator facility at CERN. As depicted in Fig.1, some part of these collisions may traverse the transition region into the quark-gluon plasma regime. Formation of a quark-gluon plasma, a deconfined state of quarks and gluons,¹ is the major focus of relativistic heavy ion experiments at higher energies. For this purpose the Relativistic Heavy Ion Collider (RHIC)² and associated experiments are presently under construction at Brookhaven for operation in 1999, and operation with heavy ions is also being planned for the LHC at CERN in 2005. As seen in the phase diagram, the anticipated temperature and density trajectories at RHIC (and for LHC heavy ions) are expected to lie close to that of the early universe, while those at the AGS and SPS occur at higher baryon densities.

A quark-hadron phase transition is predicted to have occurred at around ten micro-seconds after the Big Bang when the universe was at a temperature of approximately 150 to 200 MeV. This is the same transition as that from hadronic matter to a quark-gluon plasma, but in the reverse direction by cooling from a higher temperature as depicted in the phase diagram. Also

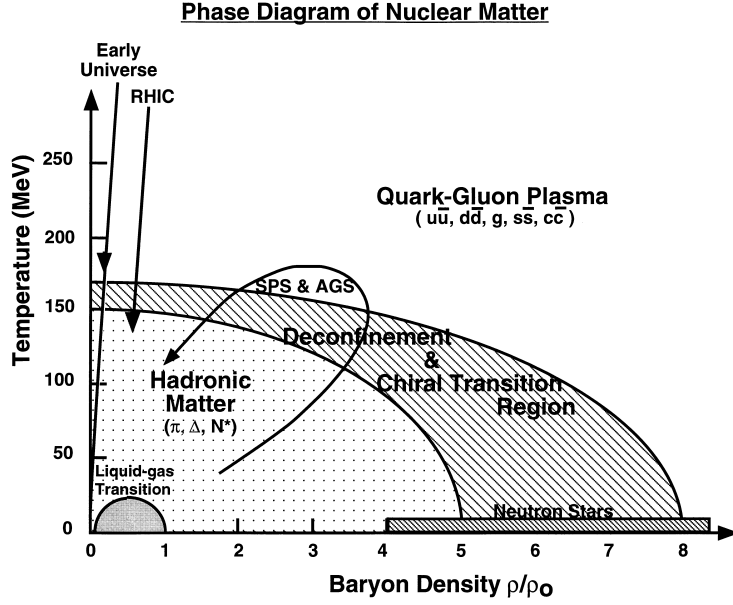


Figure 1: Schematic phase diagram of nuclear matter.

of interest in cosmology is general nucleosynthesis and the long-term effects of the possible existence of fluctuations in the quark-hadron phase transition. The region of high baryon densities and very low temperatures is important for various aspects of stellar evolution. The nuclear matter equation of state governs neutron star collapse and supernova expansion dynamics.

Collisions of relativistic heavy ions are expected to allow an investigation of the perturbative vacuum of Quantum Chromo-Dynamics (QCD).³ In such studies, a better understanding of symmetry breaking mechanisms and the origin of particle masses may be found. The QCD vacuum is predicted to have a complex internal structure, made up of a quark-antiquark condensate sea. This sea possesses energy and mass, and can undergo fluctuations about its zero point. However, isolated quarks are not expected. At low energy densities, quarks and gluons are confined in hadrons (baryons and mesons). Here the vacuum acts as a color dielectric. At the high temperatures anticipated in high energy collisions of heavy ions, the quark-antiquark condensate vacuum is expected to melt. The hadrons dissolve into freely propagating quarks and gluons, and the vacuum becomes a color conductor, or the true perturbative

QCD vacuum. This is the quark-gluon plasma (QGP) phase. At such high temperatures another phase transition is predicted to accompany the QGP transition, this is the restoration of chiral symmetry. Thus, in order to understand the phase diagram at high energy densities (high temperature and/or baryon density) and the concepts of mass and symmetry breaking, it is important to review a few of the basic concepts of Quantum Chromo-Dynamics (QCD), the theory of strong interactions.

1.1 Confinement and Deconfinement in QCD

There are two remarkable features of QCD.⁴ At large distances or small momentum transfer (Q^2), the strong coupling constant (α_s) is large and quarks are confined in colorless particles. At short distances or large momentum transfer, the coupling constant is small. This is the regime of asymptotic freedom. Measurements of the strong coupling constant which depict this behavior are presented in Fig.2.

QCD thermodynamics can be calculated on a lattice by carrying out non-perturbative numerical calculations of thermodynamic variables in QCD. The results of a calculation incorporating two light quark flavors,⁵ is displayed in Fig.3. A phase transition from a confined phase (hadronic matter) to a deconfined phase (quark-gluon plasma) is predicted to occur at a temperature of approximately 150 MeV.

A smooth but rapid transition is observed for the energy density ϵ , while a more gradual transition is observed for the pressure P , as a function of temperature T . This phase transition is either a weak first order one or a second order transition for finite lattice sizes. The large value in the difference ($3P - \epsilon$) suggests that a sudden increase in entropy density should occur in crossing the transition temperature. Lattice QCD calculations which incorporate more than two quarks predict a first order phase transition.

1.2 Chiral Symmetry

The mass of a quark depends upon the distance over which it is probed by a second quark or antiquark. Constituent quarks are dressed in a virtual cloud of quark-antiquark pairs and gluons. Since three nonrelativistic constituent quarks make up the nucleon, the constituent quark mass should be approximately one third the mass of the nucleon, or ~ 300 MeV. The shorter the distance between quarks, the smaller the mass, since the interaction weakens at short distance. Thus the current quark, which is in the regime of asymptotic freedom, is nearly bare (i.e. has near zero mass). The best estimate for the up-quark mass is approximately 5 MeV and that for the down-quark is

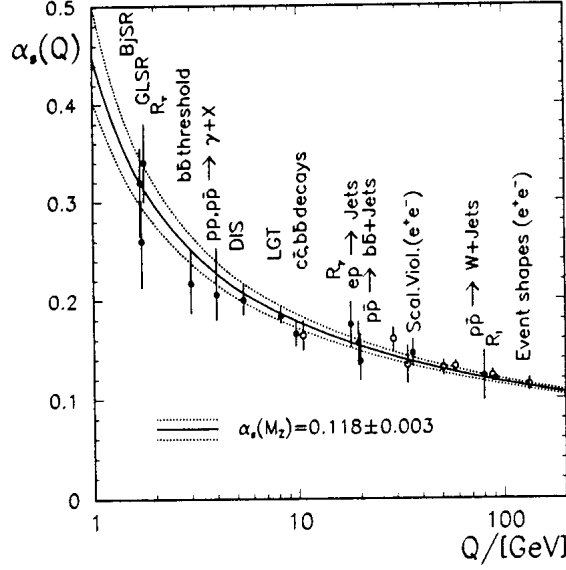


Figure 2: Compilation⁶ of experimentally determined values of the strong coupling constant α_s as a function of the momentum transfer Q^2 . The single value quoted here for α_s is the value measured at the mass of the Z^0 which is known to an accuracy of 3 percent.

approximately 7 MeV. If in fact, the light quark masses were zero, then the quarks and their composite particles would obtain another symmetry, helicity.

Massless particles have helicity, defined as the projection of the spin of the particle onto its momentum vector. Helicity is either left- or right-handed. Since massless particles travel at the speed of light, the helicity cannot change when boosting the particle to other frames, since the boost must always be less than the speed of light. Thus, the emission and absorption of vector gluons by color charges do not change the helicity of the particle. Another way of seeing this is that the QCD Lagrangian for massless quarks factorizes into a left-handed term and a right-handed term, and is therefore chirally symmetric. One term is the QCD Lagrangian for left-handed quarks and the other is that for right-handed quarks. Each can be represented by the special unitary group for isospin, i.e. $SU_L(2)$ for left-handed or $SU_R(2)$ for right-handed quarks, as appropriate, where $SU(2)_L \times SU(2)_R$ is a fundamental symmetry. Most obvious is the case of the nucleon, which cannot have helicity as a conserved quantity since its mass is non-zero, and therefore we say that chiral symmetry

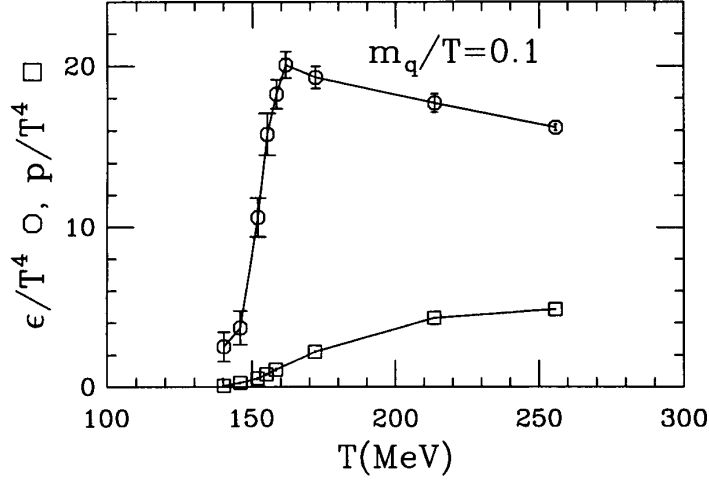


Figure 3: Results of a lattice QCD calculation using two light quark flavors.⁵ Plotted are the energy density ϵ/T^4 (circles) and the pressure P/T^4 (squares) as a function of the temperature T . A phase transition is observed in the calculation at $T \approx 150$ MeV.

is spontaneously broken. More technically, in this case the QCD Lagrangian has an additional term which is proportional to the light quark mass times the vacuum expectation value of the quark-antiquark condensate. Since this expectation value is finite, the Lagrangian cannot be chirally symmetric.

In summary, at low energy densities quarks and gluons are bound into colorless objects, called hadrons, and are confined. The quarks obtain large effective masses ($m_u \sim m_d \sim 300$ MeV, $m_s \sim 500$ MeV) by interactions among themselves and with the surrounding vacuum. This is called broken chiral symmetry. At sufficiently high energy densities, which we expect to create in relativistic heavy ion collisions, a phase transition should occur where partons become deconfined and their masses decrease ($m_u \sim m_d \sim 0$, $m_s \sim 150$ MeV) and chiral symmetry is partially restored.

1.3 Space-time Evolution of RHI Collisions

Lattice QCD calculations predict that a deconfinement transition to a quark-gluon plasma should occur at sufficiently high energy densities. Such a transition must have existed about 10 microseconds after the Big Bang. It may exist in the cores of dense stars. Can we make it in the laboratory? This

is the task of relativistic heavy ion physics, to explore QCD in the high density regime and to search for the quark-gluon plasma.

Various computer simulations of the space-time evolution of these collisions predict that the energy densities in collisions at RHIC and the LHC should surpass the threshold for QGP production over a sufficiently large volume of matter for as long as 5 - 10 fm/c in duration.^{7,8} The strength of potential QGP signals relative to the background created by the hot hadronic phase and any modifications due to final state interactions will be determined by the characteristics and time evolution of each of the following: the collision process at the parton level, formation of a QGP, expansion, cooling, and hadronization. The dynamics of these collisions can only be established once experimental measurements become available. Only then will the space-time evolution be determined, signals verified and further understanding of the transience of the state of the QGP attained.

1.4 QGP and Chiral Transition Signatures

Thermodynamic Variables

Although detailed knowledge of the collision process has yet to be obtained, there are predictions for possible signatures of QGP formation and of partial restoration of chiral symmetry. One group of QGP signatures can be classified as thermodynamic variables. This class involves determination of the energy density ϵ , pressure P , and entropy density s of the interacting system as a function of the temperature T and the baryochemical potential μ_B . Experimental observables can be identified with these variables and thus their relative behavior can be determined. If a phase transition to QGP occurs, a rapid rise in the effective number of degrees of freedom, expressed by ϵ/T^4 or s/T^3 , should be observed over a small range of T as observed in Fig.3. The variables T , s , and ϵ , can be identified with the average transverse momentum $\langle p_T \rangle$, the hadron rapidity density dN/dy , and the transverse energy density dE_T/dy , respectively.⁹ The behavior of these observables should be established in the initial round of relativistic heavy ion collider experiments.

Electromagnetic Probes

Electromagnetic (EM) probes, such as photons and leptons (i.e. virtual photons), provide information on the various stages of the interaction without modification by final state interactions. These probes may provide a measure of the thermal radiation from a QGP, if a region of photon energy, or equivalently lepton pair invariant mass, can be isolated for emission from a QGP

relative to other processes. However, the yields for EM probes are small relative to background processes, which are primarily EM decays of hadrons and resonances. Lepton pairs from the QGP are expected to be identifiable in the $1 - 1.5$ GeV invariant mass range.¹⁰ At somewhat higher masses the Drell-Yan process dominates and is expected to exceed the thermal yield of lepton pairs. There is an indication from parton cascade calculations¹¹ that lepton pairs from a QGP may dominate over Drell-Yan for even higher masses in the $5 - 10$ GeV region. This could allow one to probe the early evolution of the QGP independent of dynamical model.¹²

At lower invariant masses between 0.5 and 1 GeV, lepton pairs from hadronic sources are expected to dominate and provide information on possible medium modifications of hadrons at high density.^{13,14} The widths and positions of the ρ , ω , and ϕ peaks in the lepton pair invariant mass spectrum are expected to be sensitive to medium-induced changes of the hadronic mass spectrum, especially to a drop of vector meson masses preceding chiral symmetry restoration.^{15–23} A change in the K-meson mass would also affect the width of the ϕ -meson.^{24,25} A double ϕ peak in the lepton pair spectrum would be indicative of a long-lived mixed phase.²⁶

In fact, if the thermal fireball lives significantly longer than the ~ 1 fm/ c lifetime of the ρ -meson, then the strength of the ρ -meson in the lepton pair mass spectrum is expected to increase relative to the longer-lived ω . Thus, the ρ/ω ratio could serve as a “clock” for the lifetime of the thermal fireball.²⁷

A hadron gas and a QGP near the critical temperature are expected to emit photon spectra that are very similar in intensity and shape. If an extremely hot QGP is formed initially, photons in the transverse momentum range $2 - 5$ GeV/ c should be emitted from this hot QGP phase.^{12,28,29} Lower momentum photons are expected to be emitted primarily from the mixed phase.

Charmonium Suppression

The production of J/ψ particles in a quark-gluon plasma is predicted to be suppressed in a QGP.³⁰ This is a result of the Debye screening of a $c\bar{c}$ pair, initially formed in the QGP by fusion of two incident gluons.³¹ Less tightly bound excited states of the $c\bar{c}$ system, such as ψ' and χ_c , are more easily dissociated and will be suppressed even more than the J/ψ . Similar arguments can be made for the heavier $\Upsilon(b\bar{b})$ system.³² However the temperature at which the Υ ground state “melts” is predicted to be around 2.5 times the transition temperature, and that of the larger Υ' state only slightly above the transition temperature.

Strangeness Enhancement

A long-standing prediction for a signature of QGP formation is the enhancement of strange hadrons. The production of strange hadrons relative to nonstrange hadrons is suppressed in hadronic reactions.³³ This suppression increases with increasing strangeness content of the hadron. In a QGP the strange quark content is rapidly saturated by $s\bar{s}$ pair production in gluon-gluon reactions, resulting in an enhancement in the production of strange hadrons.³⁴ Thus, multi-strange baryons and strange antibaryons are predicted to be strongly enhanced when a QGP is formed.^{35,36} Furthermore, it has been shown^{36,37} that an enhanced strangeness content cannot be destroyed nor generated by interactions during expansion and freezeout.

Disoriented Chiral Condensates

The temporary restoration of chiral symmetry during a relativistic heavy ion collision could result in the formation of domains of a disoriented chiral condensate (DCC).³⁸ This term describes a coherent excitation of the pion field corresponding to a local misalignment of the chiral order parameter $\langle\bar{\psi}\psi\rangle$. Such domains would decay into neutral and charged pions, favoring pion ratios N_{π^0}/N_{π} substantially different from 1/3. This could also explain why final states with a large fraction of charged pions over neutral pions, observed in Centauro events,³⁹ can occur with significant probability.^{40,41} The observation of pion charge ratios significantly different from 1/3, or nonzero charge correlations,⁴² would therefore be a direct signature of the chiral phase transition.

Domains of disoriented chiral condensate may also contribute to antibaryon production through the formation of topological defects in the chiral order parameter.^{43,44} Such defects can arise at the intersection of chiral domain walls, which carry baryon number and eventually evolve into baryons and antibaryons, possibly leaving a signature of the chiral phase transition in regions of phase space that are normally baryon-poor.⁴⁵

High Pt Probes of QCD

The color structure of QCD matter can be probed by its effects on the propagation of a fast parton.^{46,47} The mechanisms are similar to those responsible for the electromagnetic energy loss of a fast charged particle in matter: energy may be lost either by excitation of the penetrated medium or by radiation.

The connection between energy loss of a quark and the color-dielectric polarizability of the medium can be established in analogy with the theory of electromagnetic energy loss.^{48,49,50} Although radiation is a very efficient energy loss mechanism for relativistic particles, it is strongly suppressed in a dense medium by the Landau-Pomeranchuk effect.⁵¹ The QCD analog of this effect has recently been analyzed comprehensively.^{52,53} Adding the two contributions, the stopping power of a quark-gluon plasma is predicted to be higher than that of hadronic matter.

A quark or gluon jet propagating through a dense medium will not only lose energy but will also be deflected. This effect destroys the coplanarity of the two jets from a hard parton-parton scattering with the incident beam axis.^{54,55} The angular deflection of the jets also results in an azimuthal asymmetry. The presence of a quark-gluon plasma is also predicted to enhance the emission of jet pairs with small azimuthal opening angles.⁵⁶ The sharp increase in the acoplanarity of di-jet events in proton-nucleus interactions observed at Fermilab⁵⁷ indicates that the interpretation of these signals is complicated by re-interaction.

2 Relativistic Heavy Ion Physics at the BNL-AGS and CERN-SPS

The experimental programs in relativistic heavy ions using the BNL-AGS and CERN-SPS started in 1986. At BNL ion beams of silicon and gold, accelerated to momenta of 14 and 11 GeV/c per nucleon, respectively, have been utilized in approximately 10 fixed-target experiments. There have been approximately 15 heavy ion experiments at CERN utilizing beams of oxygen at 60 and 200 GeV/c per nucleon, sulphur at 200 GeV/c per nucleon and Pb at 160 GeV/c per nucleon.

A presentation of selected experimental results addressing the space-time evolution of these collisions and the transition signatures will be made in this section. For a more detailed compilation of recent data, please see Refs. 86, 87.

2.1 Space-time Evolution of RHI Collisions, Thermodynamic Variables and Strangeness

Various types of measurements provide information on the dynamics of the collision process and the thermodynamic variables of the interacting system, such as the energy density ϵ , pressure P , entropy density s , temperature T and the baryochemical potential μ_B . The nuclear stopping power can be defined as the degree to which the energy of relative motion of the incoming nuclei

is transformed into other degrees of freedom. The stopping power determines the amount of energy accessible in the interaction region, the volume of the interaction region and therefore the energy density (which is the energy divided by the volume of the interaction region). These values change as the system evolves and thus a significant difficulty is to determine these parameters as a function of time.

The nuclear stopping power influences the dynamics of the reaction process and as a result it also determines whether conditions are favorable for a deconfinement transition or a chiral transition. It can be measured in various ways. The energy remaining in the forward direction of the collisions can be measured using forward calorimetry along the initial beam direction. The difference between the energy remaining in the forward direction and the initial energy of the beam provides a measure of the energy that has been transformed into other degrees of freedom, such as QGP formation and eventual particle production. Another measurement, that of the amount of transverse energy after the collision, provides an indication of the energy transformed into particle production. A third type of measurement is the determination of the final-state rapidity distributions of protons. This is a measure of the redistribution of the incident protons (and thus the valence quarks) into the final state as a result of the collision process. This is a measure of how the valence quark distributions evolve from the incident to the final state in the collision process.

Measurements have been made using various nuclear systems at the AGS and SPS. The results indicate that the amount of nuclear stopping power is large. The experiments measure transverse energy densities of up to 200 GeV per unit pseudorapidity at the AGS⁵⁸ and up to 450 GeV at the SPS⁵⁹ in central collisions of heavy nuclei (Au or Pb). Taking the measured transverse energy densities and the system volume calculated using a Bjorken longitudinal expansion geometry,⁶⁰ the energy densities can be derived. These results indicate that the amount of energy in the interaction region is sufficient to produce energy densities well above the critical energy density predicted by lattice QCD calculations⁶¹ ($\epsilon_{crit} \sim 1.5 \text{ GeV}/fm^3$ for the deconfinement transition).

In interpreting this value, one must keep in mind the complications of deriving an energy density which changes rapidly as a function of time during the collision process. The present approach takes the total measured transverse energy and divides by the volume of the system derived from Bjorken longitudinal expansion. The actual energy density can be larger at specific locations of the interaction region and smaller at others. A complex issue which is yet to be resolved is a determination of the energy density as a function of space and time during the collision process. This will involve a combination

of high quality triple differential cross section measurements and dynamical calculations which include all prominent processes.

Additional information can be derived from the rapidity distributions of baryons in the final-state. This has been performed at both the AGS and SPS. Results from the heaviest system (Pb + Pb) at the highest energy (158 GeV/c per nucleon) indicate that the stopping power is indeed extremely large, as is the case with the transverse energy measurements. Displayed in Fig.4 are data from the NA49 Collaboration⁶² which exhibit clearly this large degree of stopping. The baryon - antibaryon distributions, which reflect the distribution of final-state valence quarks, are peaked at midrapidity. This signifies that the incident baryons (nucleons) experience significant stopping, slow-down, pile-up at midrapidity and are then ejected over a broad peak or plateau at midrapidity (90 degrees in the c.m. frame). This can be contrasted with the same measurement in the lighter S + S system,⁶³ also shown in Fig.4 and scaled by a factor of 7 for comparison. The baryon - antibaryon distribution in the lighter system exhibits peaks between the initial target and beam rapidities (located at 0 and 6, respectively, in the figure) and midrapidity (located at 3). Thus, in the lighter system the incident baryons (nucleons) experience less stopping and are not displaced as far away from their initial rapidities as in the heavier system. Data from the NA44 Collaboration⁶⁴ at the SPS are consistent with the NA49 Pb + Pb measurement. The E866^{65,66} and E877^{67,68} Collaborations have performed similar measurements for the Si + Al and Au + Au systems at the AGS with strikingly similar results and conclusions.

Measurements of the cross sections for the production of various types of particles as a function of transverse momentum and rapidity can provide information on the space-time evolution of the collisions. In addition to the rapidity distributions of the net baryons described above, distributions of the more abundantly-produced light particles, which are primarily pions and kaons, provide much important information on the dynamics of the collision process. The rapidity distributions measured for pions and kaons in the heaviest systems, peak at midrapidity and for pions is much broader than a thermal distribution at the highest (saturated) temperature for both the AGS^{66,68} and SPS^{69,70} energies. An interesting difference emerges for the two energies when comparing the measured pion to participant baryon ratios. The value measured for Pb + Pb at the SPS is approximately 6, while that measured for Au + Au at the AGS is near unity. This is a significant difference which reflects an extremely large increase in entropy density in going from the lower AGS energy to the higher SPS energies. This increase in the entropy density and its behavior as a function of energy will be studied and correlated with other measurements when the SPS operates at lower energies in the near-future to understand the

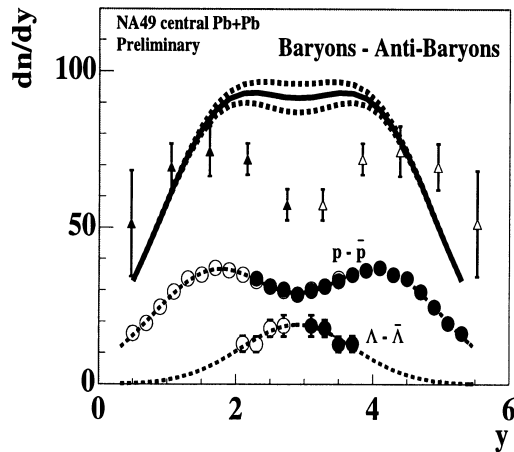


Figure 4: The rapidity distributions for baryons - antibaryons (solid curve) derived from the $p - \bar{p}$ and $\Lambda - \bar{\Lambda}$ distributions shown and labeled in the figure. The dashed curve represents the errors on the derived baryon - anti-baryon distributions. For comparison, a similar measurement for S + S is scaled by a factor of 7 and displayed as triangles. See the text for discussion. Solid symbols represent the measured points and open symbols are these same points reflected about midrapidity (symmetry axis).

systematics that evolve between the energies of the AGS and SPS.

In general, transverse momentum or transverse mass, defined as $m_{\perp} = (m^2 + p_{\perp}^2)^{1/2}$, distributions provide information on the evolving system integrated over time. For hadrons the spectra provide information on a superposition of scattering phenomena. These include semi-hard and hard scattering processes leading to hadrons after parton fragmentation at high transverse momenta, rescattering and thermalization leading to a thermal-like spectrum at low transverse momentum (up to about twice the particle mass), and a range of processes in between. Most notable of these other processes is collective flow, which manifests itself in the spectra at low and intermediate momenta up to several times the particle mass. The measurements of the transverse mass distributions at the AGS^{66,68,71} and SPS^{69,70,72} have focussed on the low and intermediate mass region where thermal and collective flow effects dominate, since hard scattering effects are small at these energies. The resultant measurements exhibit invariant transverse mass distributions which are primarily exponential in form, i.e. $(1/m_{\perp})dn/dm_{\perp} \sim e^{-m_{\perp}/T}$, at a given rapidity. The inverse-slope parameters (T) increase linearly with the mass of the detected particle for a given colliding system (energy, mass and impact parameter).^{62,73}

An example of this dependence is shown in Fig.5. As can be seen in Fig.5, the inverse-slope parameters become rather large. Clearly, such large values of T cannot be associated with temperatures of the hadronic system at freeze-out, since they are higher than the predicted QGP transition temperature and hadrons could not exist at these temperatures. Detailed studies^{74,75} indicate that the linear increase of the inverse-slope parameters with the particle mass is a result of the strong influence of collective flow, which is a product of pressure gradients in the system.

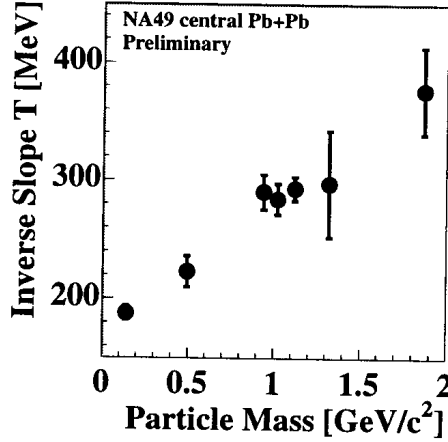


Figure 5: Inverse-slope parameters derived from the invariant transverse mass distributions for various hadrons plotted as a function of the particle mass for central Pb + Pb collisions at 158 GeV/c per nucleon.

The various effects of collective flow in these collisions have been studied in more detail and have recently been presented in Ref. 76. The simplest approach involves fitting the transverse mass distributions with two parameters using a thermal freeze-out component (represented by the parameter T_{fo}) and a transverse flow velocity profile as a function of transverse radius (r) of the form $\beta_{trans}(r) = \beta_{max} r / R_{max}$. The second parameter β_{max} is the strength of the maximum transverse flow velocity at the radius (R_{max}) for all particles.^{74,75} Fitting the transverse mass distributions using the two parameters in this approach leads to a correlation in the parameters and a range of possible parameter values. A typical range of values which results in good fits for the transverse mass distributions in central collisions of Pb + Pb at the SPS are $(T_{fo}, \beta_{max}) = (120 \text{ MeV}, 0.6)$ to $(140 \text{ MeV}, 0.45)$. One sees that there is some flexibility in the fit procedures which results in a trade-off in the values of the

two parameters.

Various approaches have been utilized to resolve this ambiguity in the values of (T_{fo}, β_{max}) . One approach is to use two-particle Bose-Einstein interferometry to impose a more stringent restriction on the values of (T_{fo}, β_{max}) when fitting the data. This has been performed by the NA49 Collaboration utilizing the constraints imposed by fitting the single-particle transverse mass distribution for negative hadrons and that for deuterons, along with the dependence of the two-pion correlation function on the relative momentum of the pion pair.⁷⁷ This works because there is a dependence of the two-particle correlation function on the average momentum of the particle pair, which reflects the correlation between the momentum and position of the particles during the expansion.⁷⁸ Therefore, one can map out the allowed values of the freeze-out temperature and transverse flow velocity in a manner that more tightly constrains these parameters. This analysis results in the values $(T_{fo}, \beta_{max}) = (120 \text{ MeV}, 0.55)$. Using a different model for the dependence of the two-particle interferometry on the space and momentum correlation, the NA44 Collaboration obtains the values $(T_{fo}, \beta_{max}) = (140 \text{ MeV}, 0.4)$.⁷³ The use of more sophisticated model calculations, such as hydrodynamic models or RQMD,⁷⁹ to determine the space-momentum correlations and compare with the data, should provide additional insight into the space-time evolution of these collisions. In addition, further exploitation of the various parameters of the two-particle correlation function could lead to additional information about the collision process.⁷⁸

A better indication of the degree of thermal and chemical equilibration in the system can be gained from the study of the relative abundances of the various particles that are produced in these interactions. Several studies^{80,81,82,83} have compiled the particle ratios measured in experiments at the AGS and SPS and compared these with thermal and chemical equilibrium models. It is concluded that a large degree of chemical equilibration occurs in these collisions.⁸⁰ In fact, reasonable agreement between a thermal model and the data on particle abundances is found with complete chemical equilibration, including saturation of strangeness ($\gamma_s = 1$), and utilizing temperature and baryochemical potential parameters in the range $(T, \mu_B) = (160, 200)$ to $(175, 270)$ in units of MeV for reactions at the SPS.⁸⁴ Thus, there is evidence at the SPS energies that the chemical freezeout occurs at higher temperatures than thermal freezeout. Thus, the abundances of the various particles are established earlier and at a higher temperature than the final particle momenta, which are determined at thermal freezeout. Similar analysis of the AGS data yields $\mu_B = 540 \text{ MeV}$ and $T = 120 - 140 \text{ MeV}$, with the system in complete equilibrium.⁸⁰

The NA44 Collaboration have found that the particle abundances which they measure are well fit by a thermo-chemical model with $\mu_u = \mu_d = 75 - 85$ MeV, $\mu_s = 22 - 31$ MeV, $T = 155 - 170$ MeV and $\gamma_s = 0.75 - 0.95$, where μ_q are the up, down and strange quark chemical potentials, T is the temperature, and γ_s is the strangeness saturation factor.⁸⁵ Thus, they find somewhat different parameters than the previous analysis and only partial chemical equilibrium for strange particles. An analysis of the NA49 data utilizing a statistical model of a hadron gas⁸² also yields only partial equilibrium in the strangeness degree of freedom with $\gamma_s = 0.6$. It is therefore still too early to establish definitively these parameters from the data, although the range of parameters that result are particularly interesting in pinning down the locus of T and μ_B in the phase diagram. It appears that a better understanding of strangeness production is necessary before determination can be made about whether strangeness is equilibrated, since the models still have difficulty in fitting some of the strange particle abundances.

2.2 QGP and Chiral Transition Signatures

Charmonium Suppression

Charmonium production is expected to be suppressed in a QGP³⁰ relative to hadronic matter. The NA50 Collaboration at CERN has measured the production of J/ψ and ψ' in 158 GeV/c per nucleon Pb + Pb reactions using a muon pair spectrometer. They observe an anomalous suppression of the J/ψ and ψ' ,⁸⁸ normalized to Drell-Yan pair production, in comparison to the suppression already measured in lighter systems with proton, oxygen and sulphur induced reactions in NA38.⁸⁹ Shown in Fig.6 is the opposite-sign muon pair mass spectrum. A peak resulting from decays of the J/ψ and a bump from the ψ' decays can be seen in the spectrum. The fit to the data is superimposed on the spectrum with the various components of the fit depicted and labeled individually. For example, the underlying Drell-Yan and open charm backgrounds are depicted in the figure. The fit is performed above a dimuon mass of 3.05 GeV/c². The fit requires five parameters - J/ψ amplitude, ψ' amplitude, Drell-Yan amplitude, and the mass and width of the gaussian line shape of the J/ψ - and includes the spectrometer resolution. The ψ' mass and width are derived from those for the J/ψ . For more details of the fit, see Ref. 88.

Analyses of the NA38 and NA50 data indicate that the nuclear dependence of the Drell-Yan cross section on the mass of the colliding system (with A target nucleons and B projectile nucleons) can be parameterized as $\sigma^{AB} = (AB)^\alpha \sigma^{NN}$, with $\alpha(DY) = 1.002 \pm 0.001$.⁹⁰ This suggests the lack of nuclear

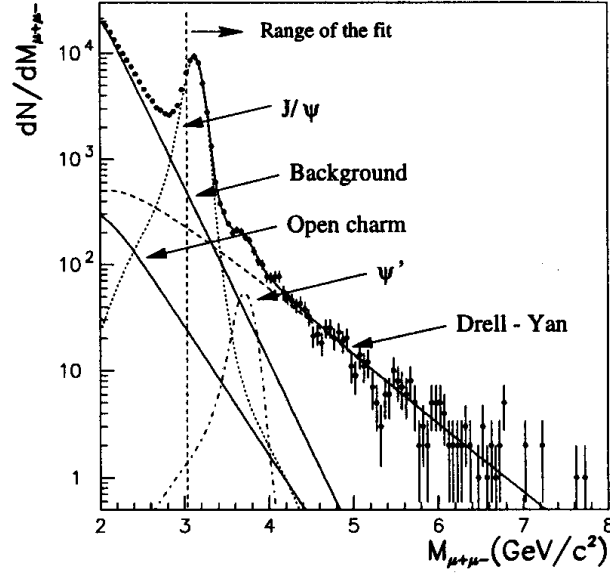


Figure 6: Opposite-sign muon pair mass spectrum measured in the CERN NA50 experiment. For details about the data and the superimposed fits, see the text.

absorption in these hard processes. When the same approach is applied to the J/ψ production data for proton, oxygen and sulphur induced reactions, a value of $\alpha(J/\psi) = 0.92 \pm 0.015$ is found. The observed nuclear effect is consistent with absorption of a pre-resonant $c\bar{c}$ system in nuclear matter.⁹¹ In contrast, for the heaviest system Pb + Pb a value of $\alpha(J/\psi) = 0.74 \pm 0.04$ is measured for J/ψ production. This suggests an anomalous suppression⁹⁰ of the J/ψ for the heaviest system.

Since the Drell-Yan cross section scales as $A \times B$, it can be used to represent the number of parton-parton collisions. Thus, σ^{DY} can be used to normalize between measurements with different systems and impact parameters. The ratio of $\sigma^{J/\psi}/\sigma^{DY}$ can then be plotted for the various measurements at a given (or properly normalized) energy. The NA50 Collaboration defines a geometrical mean path length $\bar{L}(b)$ of the $c\bar{c}$ system traveling through nuclear matter for each nuclear reaction at a given impact parameter b , which is derived for each collision assuming a geometrical model and using the transverse energy measured in the experiment. This is calculated using a monte carlo technique for determining $\bar{L}(b) = \langle \rho L \rangle / \rho_0$, where ρ is a standard Woods-Saxon nuclear

density distribution, ρ_o is normal nuclear matter density, and L is the sum of the path length of the $c\bar{c}$ system through the remnants of each of the nuclei. The ratio of $\sigma^{J/\psi}/\sigma^{DY}$ times the branching ratio to muon pairs $B_{\mu\mu}$ is plotted in Fig.7 as a function of L in fermi. The proton, oxygen (not shown) and sulphur induced reactions are well reproduced by the straight line fit in the figure, which represents $B_{\mu\mu}\sigma^{J/\psi}/\sigma^{DY} = \exp(-\rho\sigma_{abs}L)$ with $\sigma_{abs} = 6.2 \pm 0.7mb$ for normal absorption of a $c\bar{c}$ state. The most peripheral Pb + Pb data agree with the normal absorption model. However for $L > 7.5$ fm the Pb + Pb data are suppressed strongly by factors as large as 0.62 ± 0.04 .

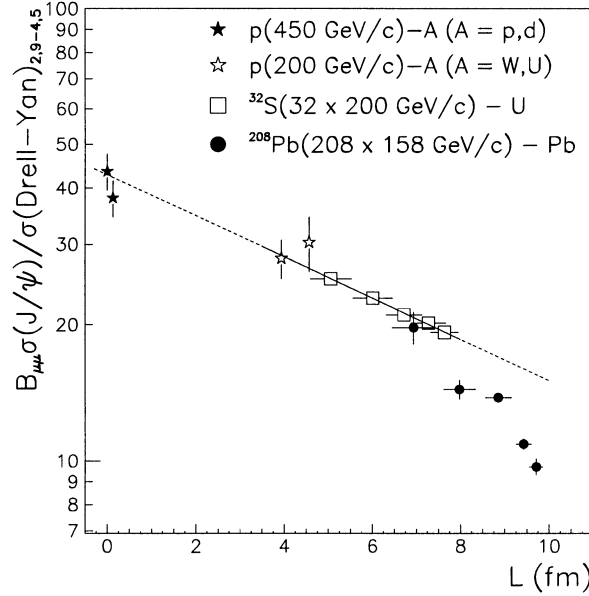


Figure 7: The ratio $B_{\mu\mu}\sigma^{J/\psi}/\sigma^{DY}$ plotted as a function of the geometrical mean path length $L(b)$ of the $c\bar{c}$ system traveling through nuclear matter for the various colliding nuclear systems. See text for details.

Higher statistics data, which have been reported recently by NA50,⁸⁸ support this observation with greater significance and more detail in impact parameter definition. Furthermore, similar data has been taken for the ψ' channel showing an anomalous suppression which appears not only for low impact parameter Pb + Pb collisions, but also in low impact parameter S + U collisions. The anomalous suppression occurs for J/ψ geometrical mean path lengths of $L > 8fm$ and for $L > 5fm$ for the ψ' . This is consistent with the expectation

that the ψ' should break up more readily in matter than the J/ψ , since the ψ' has a larger radius. The largest suppression of J/ψ is found to be most prevalent for J/ψ with low transverse momentum ($p_{\perp} < 1.5 - 2.0$ GeV/c). Predictions of models incorporating absorption in co-moving hadronic matter^{92,93,94} and those including deconfinement⁹⁵ are presently being compared to the data. The NA50 Collaboration finds that those models incorporating only co-movers cannot reproduce the anomalous suppression measured in the J/ψ and ψ' data sets. Further theoretical and experimental work is needed to determine definitively the origin of the observed suppression. In the two types of models which require co-movers or deconfinement, high density (hadronic or partonic) matter is needed to reproduce even the normal suppression observed in all colliding systems.

2.3 Electromagnetic Probes

Lepton Pairs

Real and virtual photons in the form of lepton pairs are an excellent probe of the early stages of the interaction, since they escape the interaction region without subsequent interaction or modification due to the final state of the interaction. Various measurements have been made utilizing ion beams on nuclear targets at the CERN SPS. The CERES/NA45 Collaboration has measured an enhancement of electron pairs⁹⁶ above that expected from hadronic sources in the mass region around the ρ meson, specifically $0.2 < m_{ee} < 1.5$ GeV/ c^2 . These measurements were performed in the CERES/NA45 electron spectrometer which utilizes the hadron-blind technique to measure electrons and photons. Electron pairs allow the measurement of initial quark-antiquark annihilation via the elementary $q\bar{q} \rightarrow e^+e^-$ process (relevant if a QGP is formed), pion annihilation in a high density hadronic medium via $\pi^+\pi^- \rightarrow e^+e^-$, and the leptonic decays of hadronic resonances (such as the ρ -meson). The ρ is of particular interest as it has a short lifetime compared to the interaction times and it decays very quickly in the presence of the medium (whether QGP or hadronic). Thus, it should exhibit signs of possible chiral restoration if there is a reduction of the ρ -meson mass.

The measured electron pair mass spectra of p + Be and S + Au interactions are shown in Fig.8. The spectra for p + Be can be described as a superposition of the decays of various hadrons, whose components are also shown in Fig.8. The S + Au electron pair data are enhanced relative to a superposition of electron pairs from the decays of known hadrons. These fascinating results have stimulated considerable activity among theorists in an attempt to explain the observed enhancement. The simplest interpretation consistent

with properties of the observed enhancement is that the enhancement is due to $\pi\pi$ annihilation.⁹⁷ Many calculations⁹⁸ have addressed these data utilizing $\pi\pi$ annihilation, however they all have difficulty fitting the enhancement in the electron pair data at pair masses $0.2 < m_{ee} < 0.5 \text{ GeV}/c^2$. A model has been proposed⁹⁹ which incorporates a decrease in the ρ -meson mass due to chiral restoration^{100,101} in the dense medium. It agrees with the CERES data and similar results from HELIOS-3.¹⁰² Another approach which incorporates a spectral function for the ρ , pion modification in-medium, and ρ scattering leading to a significant broadening in the ρ resonance fits the data equally well. The various theoretical approaches have recently been summarized in Ref. 103.

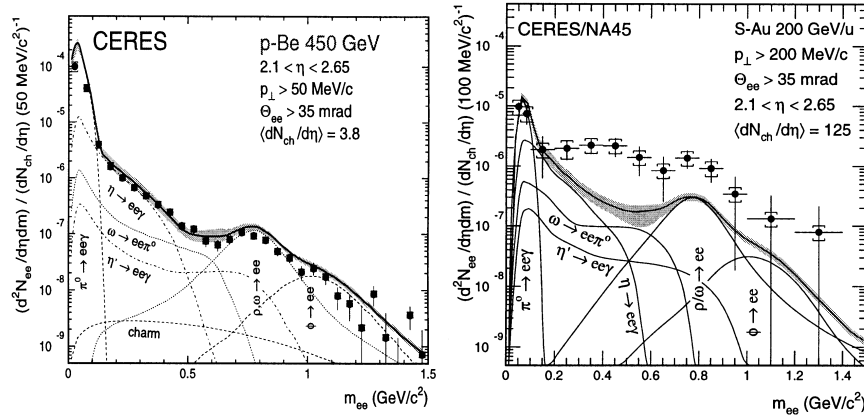


Figure 8: Electron pair (e^+e^-) invariant mass spectrum in p + Be and S + Au interactions⁹⁷ normalized by the charged particle multiplicity density. The experimental data are presented as data points, and the statistical and systematic errors are exhibited separately as error bars and brackets, respectively. The contributions from the decays of hadrons are also presented as individual curves. The curve represents the total contribution from hadronic sources, while the shaded region is the systematic error on this value. An enhancement above the sum of the contributions of electron pairs from the decays of hadrons is observed for the S + Au interactions.

The CERES/NA45 Collaboration have recently measured and analyzed the e^+e^- pair mass spectrum in Pb + Au collisions. These data are shown in Fig.9. The enhancement observed for masses above $0.2 \text{ GeV}/c^2$ in the S + Au data of Fig.8 beyond the e^+e^- yield expected from hadronic sources is also seen in these data. The enhancement factor for the mass region from $0.3 - 0.7 \text{ GeV}/c^2$ is found to be 5.8 ± 0.8 (statistical) ± 1.5 (systematic) and that for the entire mass region from $0.2 - 2.0 \text{ GeV}/c^2$ is 3.5 ± 0.4 (statistical) \pm

0.9 (systematic). For the S + Au system the enhancement factor for the mass region from 0.2 - 1.5 GeV/c^2 was found to be 5.0 ± 0.7 (statistical) ± 2.0 (systematic). Similar enhancements in the low mass spectrum of muon pairs have been observed in S + W by HELIOS-3¹⁰² and in S + U by NA38¹⁰⁴ for an incident momentum of 200 GeV/c per nucleon.

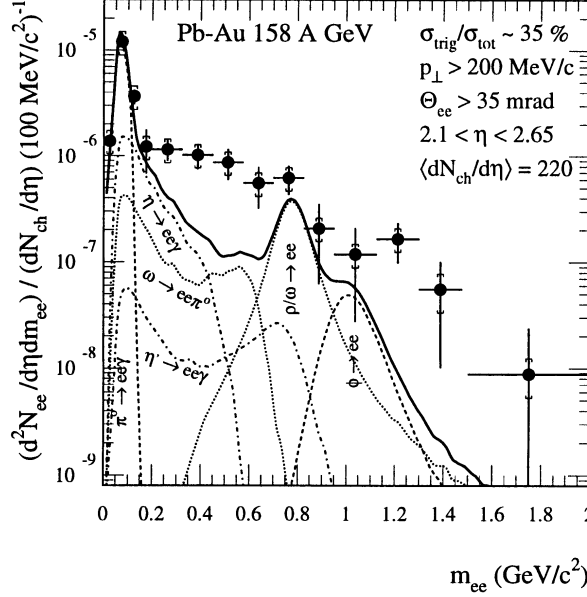


Figure 9: Electron pair (e^+e^-) invariant mass spectrum in Pb + Au interactions⁹⁶ (normalized) relative to the charged particle multiplicity density. The various components are described in the Fig.8 caption.

CERES/NA45 have also investigated whether the electron pair mass spectrum changes as a function of the event multiplicity (i.e. dependence on centrality or impact parameter). These results are shown in Fig.10. They find that in the mass region of the enhancement, i.e. for masses greater than 0.2 GeV/c^2 , the electron pair density divided by the charged particle density increases with the multiplicity density of the collision. This can be compared to what is expected for electron pair production from hadronic sources as measured in the p + Be and p + Au reactions, also plotted in Fig.10 and represented by the horizontal line. The enhancement above this line in the Pb + Au reaction is indicated on the right-hand vertical scale and reaches a value just above 5 for the highest charged particle multiplicity bin representing

the most central collisions with smallest impact parameter. The electron pair transverse momentum spectra have also been studied as a function of the pair mass. It was found that the enhancement is most prevalent for low momentum pairs of electrons. A significant upgrade of the CERES/NA45 spectrometer is underway which will allow improved mass resolution to disentangle the ρ , ω , and ϕ , and higher statistics are anticipated.

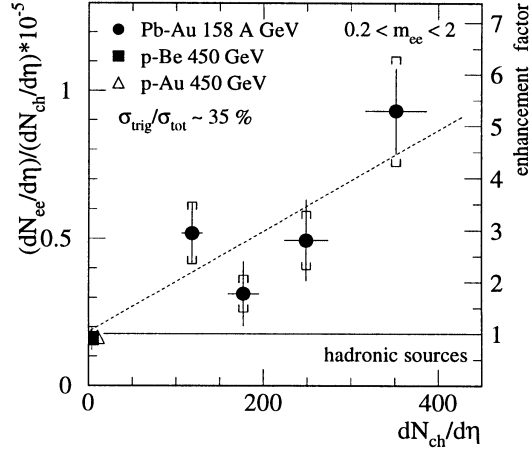


Figure 10: The ratio of the electron pair density relative to the charged particle density measured in Pb + Au interactions plotted as a function of the mean charged particle density of each ensemble of events. Also shown are the values measured in proton-induced nuclear reactions which are consistent with production from known hadronic sources (horizontal line). The scale on the right-side represents the enhancement factor above the electron pair production from known hadronic sources.

Direct Photons

Direct photons in the 2 – 5 GeV energy range may provide a measure of the thermal radiation from a QGP, if an extremely hot QGP is formed. Lower energy direct photons could be emitted from a mixed phase of QGP and hadronic matter. The CERN WA80, NA34 and NA45 experiments have performed measurements of the direct photon yield with ion beams on nuclear targets. Results of these measurements have been summarized recently.¹⁰⁵ No direct photons were observed in the CERES/NA45 measurements¹⁰⁶ nor in the NA34 experiment¹⁰⁷ with a level of approximately 10% systematic errors. The WA80 experiment¹⁰⁸ has seen a slight signal, although within their systematic errors (5%) it is consistent with no direct photons.

Thus, a significant direct photon signal has not been established in relativistic heavy ion collisions at the energies presently available from the fixed-target facilities.

2.4 Disoriented Chiral Condensates

The temporary restoration of chiral symmetry during a relativistic heavy ion collision could result in the formation of domains of a disoriented chiral condensate (DCC). Such domains would decay into neutral and charged pions, and due to fluctuations during the decay would produce pion ratios N_{π^0}/N_{π} substantially different from 1/3. The CERN WA98 experiment has measured the multiplicities of charged particles (primarily pions) and photons (primarily from the decays of neutral pions) in central Pb + Pb collisions at 158 GeV/c per nucleon.¹⁰⁹ To date they have observed no events with a large charge to neutral fluctuation from among 200K events, and report no significant DCC signal.

2.5 High Pt Probes of QCD

Measurements of the fragmentation products of hard scattering can provide information on the matter through which the hard-scattered parton propagates. Thus, the color structure of QCD matter can be probed by its effects on the propagation of a fast parton. Until recently, there has been no measurement at the AGS nor SPS which is relevant to this probe. It has been thought that hard scattering processes do not contribute significantly in this energy regime. Only recently, has this issue been addressed quantitatively.¹¹⁰ We have yet to see what this probe will tell us at the SPS energies.

2.6 Summary of Relativistic Heavy Ion Measurements from the BNL-AGS and CERN-SPS

The results from relativistic heavy ion experiments thus far at the AGS and SPS have been quite intriguing. A large amount of stopping is observed in central collisions of the heaviest systems at the AGS and SPS. This stopping results in the transfer of a large amount of energy from the relative motion into other degrees of freedom. At SPS energies this creates high energy densities beyond those predicted for production of a quark-gluon plasma ($\epsilon \sim 1.5 - 2.0$ GeV/fm³). The actual size and space-time evolution of this high energy density regime can only be understood after further investigation using dynamical models with realistic ingredients, which reproduce the experimental observables. An increase in the pion to baryon ratio from approximately 1 to about

7 has been measured in going from the AGS to the SPS energies. This is a result of the large energy deposition. It is anticipated that measurements will be made at energies intermediate between those of the AGS and SPS to better determine and understand the evolution of the rise in entropy density and its relation to the equation of state of nuclear matter.

Thermal and chemical equilibrium models are generally able to reproduce the particle abundances and particle spectra measured in central collisions at the AGS and SPS, once the strong influence of collective nuclear flow is taken into account. As a result, the parameters which best fit the particle ratios and particle spectra, including two-particle correlations, at the SPS are found to be the freezeout temperature $T_{fo} = 120 - 140$ MeV, the maximum transverse flow velocity $\beta_{max} = 0.4 - 0.55c$ (where c is the speed of light), the temperature at chemical equilibrium $T = 160 - 175$ MeV, the baryochemical potential $\mu_B = 200 - 270$ MeV, and the strangeness saturation factor $\gamma_s = 0.6 - 1.0$. Similar values have been derived from measurements at the AGS and yield values of the temperature at chemical equilibrium $T = 120 - 140$ MeV and a baryochemical potential $\mu_B \approx 540$ MeV. Clearly, the range of values for each parameter represents work to be done to better understand the differences in the measurements and theoretical approaches which lead to these discrepancies. However, these values provide us with the first indication of the region of the parameter space that is populated in these collisions. From this there is evidence for chemical and thermal equilibrium from the results at the AGS and SPS energies. This evidence is strongest for the AGS energies and weaker, especially for thermal equilibrium, at the SPS energy. Furthermore, the issue of strangeness saturation (i.e. if $\gamma_s = 1$), which is required for deconfinement, is still to be settled.

Measurements of charmonium production exhibit a suppression of the yield of both the J/ψ and the ψ' relative to Drell-Yan production for central collisions of Pb + Pb at the SPS. Furthermore, the yield of the ψ' relative to Drell-Yan is also observed to be suppressed for central collisions of the lighter S + Pb system, whereas the J/ψ is not. These results follow the expected pattern that the Debye screening will initially affect the ψ' before the J/ψ as the energy density is raised (i.e. as in going from the lighter to the heavier system at the SPS). These results suggest that the deconfinement regime has been reached at the SPS. However, various theoretical models have recently been able to predict this behavior utilizing re-interaction and break-up of charmonium in high density matter without invoking deconfinement.

Measurements from three different experiments are consistent with no signal from direct photons due to a QGP. Electron pair (virtual photon) measurements exhibit an enhancement at low to intermediate pair masses relative to

pairs expected from hadronic decays for central collisions of the heavier systems ($S + Au$ and $Pb + Au$) at the SPS. This enhancement has stimulated considerable theoretical investigation involving $\pi\pi$ annihilation, collision broadening, in-medium effects such as a decreased ρ mass due to partial chiral symmetry restoration, and other effects. Future measurements with higher mass resolution should provide important information with which to distinguish models describing the electron pair enhancement. (In another investigation no disoriented chiral condensates have been seen.)

In summary, the quark-gluon plasma has yet to be observed unambiguously, although there have been many interesting effects of high density nuclear matter observed in the AGS and SPS experiments. This bodes well for studies using relativistic heavy ions at significantly higher energies at RHIC and the LHC.

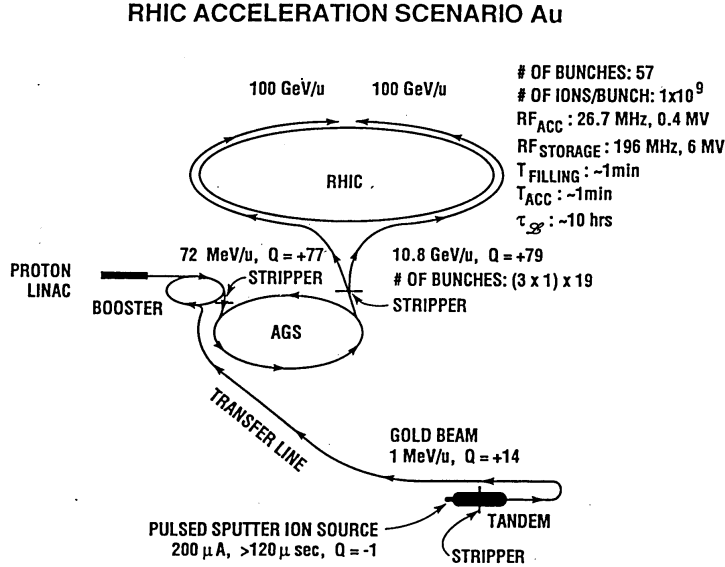


Figure 11: The Relativistic Heavy Ion Collider (RHIC) accelerator complex at Brookhaven National Laboratory. Nuclear beams are accelerated from the tandem Van de Graaff, through the transfer line into the AGS Booster and AGS prior to injection into RHIC. Details of the characteristics of proton and Au beams are also indicated after acceleration in each phase.

3 Relativistic Heavy Ion Collider and Experiments

The Relativistic Heavy Ion Collider is presently under construction and expected to begin operation for experiments in June 1999. A schematic diagram of the RHIC accelerator complex at Brookhaven is displayed in Fig.11. Nuclear beams are accelerated from the tandem Van de Graaff accelerator through a transfer line into the AGS Booster synchrotron and then into the AGS, which serves as an injector for RHIC. RHIC will accelerate and collide ions from protons up to the heaviest nuclei over a range of energies, up to 250 GeV for protons and 100 GeV/nucleon for Au nuclei. Fig.12 summarizes the capabilities of the accelerator. In addition to the colliding beams described in Fig.12, plans are underway to inject and accelerate polarized protons at RHIC in order to study the spin content of the proton.¹¹¹

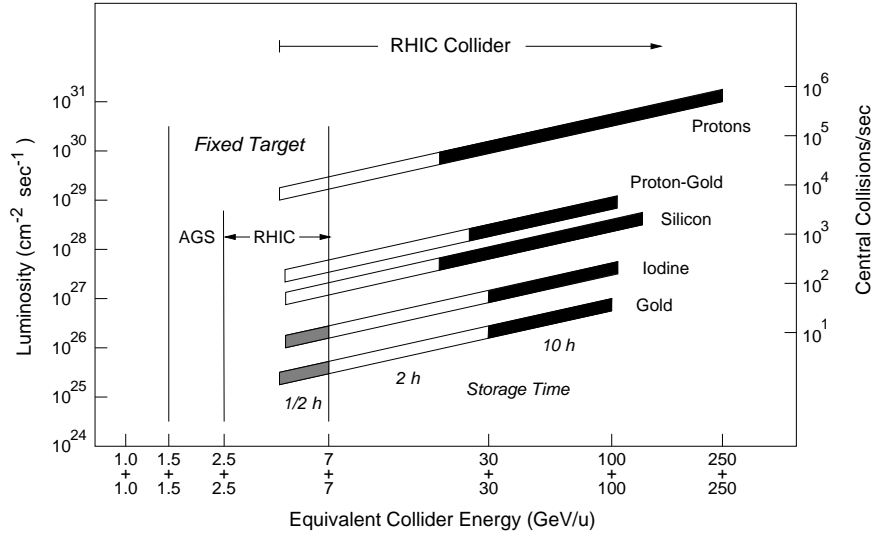


Figure 12: The RHIC luminosity and number of central collisions per second, for impact parameters less than 1 fermi, are plotted as a function of the colliding beam energies for various projectile systems.

Collisions of the heaviest nuclei at impact parameters near zero at RHIC are expected to produce around 1000 charged particles per unit pseudo-rapidity. This presents a formidable environment in which to detect the products of these reactions. The experiments will take various different approaches to search for the QGP. Two large collider detectors, STAR and PHENIX, are

under construction for operation at RHIC start-up. The STAR experiment will concentrate on measurements of hadron production over a large solid angle in order to study global observables on an event-by-event basis. The PHENIX experiment will focus on measurements of lepton and photon production and will have the capability of measuring hadrons in a limited range of pseudorapidity. In addition, two smaller experiments are under construction. These are BRAHMS, a forward and midrapidity hadron spectrometer, and PHOBOS which is a compact multiparticle spectrometer. The collaborations, which are constructing these detector systems and which will exploit their physics capabilities, consist of approximately 900 scientists from over 80 institutions internationally. An in-depth description of STAR, with which I am affiliated and most familiar, and its physics goals will be presented. Then a summary description of each of the PHENIX, PHOBOS and BRAHMS experiments and their physics goals will be presented.

3.1 The STAR Experiment

The STAR (Solenoidal Tracker At RHIC) experiment¹¹² is presently under construction with operation anticipated at RHIC beginning in June 1999. A schematic layout of the STAR detector systems is shown in Fig.13. The initial configuration of STAR consists of high resolution tracking detectors, trigger detectors, and partial coverage of electromagnetic calorimetry inside a 0.5 T solenoid. The solenoid provides a uniform magnetic field for tracking, momentum analysis and particle identification via ionization energy loss measurements in the tracking detectors. These measurements will be carried out at mid-rapidity, over a large pseudorapidity range ($|\eta| < 4$) with full azimuthal coverage ($\Delta(\phi) = 2\pi$) and azimuthal symmetry. The tracking detectors are a silicon vertex tracker (SVT) covering $|\eta| < 1$, a large time projection chamber (TPC) covering $|\eta| < 1.7$, and a forward radial-drift TPC (FTPC) covering $2.5 < |\eta| < 4$. In addition to the tracking detectors, the electromagnetic calorimeter (EMC) will measure the transverse energy of events, and trigger on and measure high transverse momentum photons, particles and jets. Approximately 10% of the EMC is expected to be ready for initial RHIC operation, with the remainder being constructed and installed over the three years following RHIC start-up. A time-of-flight system (TOF) surrounding the TPC to extend particle identification to higher momenta has been proposed for future construction. The following trigger detectors are under construction for STAR: a central trigger barrel surrounding the outer cylinder of the TPC for charged-particle multiplicity triggering in the $|\eta| < 1$ region, a TPC endcap trigger for triggering on charged particle multiplicity over $1 < |\eta| < 2$,

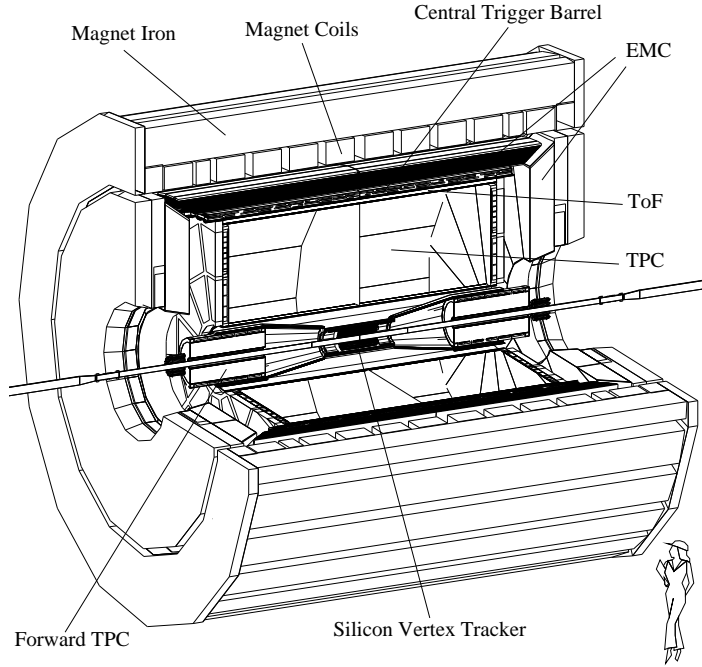


Figure 13: Layout of the STAR experiment at RHIC.

a vertex position detector to identify and localize the interaction vertex, and zero-degree calorimeters (at large pseudorapidities, not shown in Fig.13) for vetoing large impact parameter collisions with a large amount of energy remaining in the forward direction. The electronics, data acquisition and online monitoring systems for these detectors will also be installed.

STAR will search for signatures of QGP formation and investigate the behavior of strongly interacting matter at high energy density in central collisions of relativistic nuclei. The STAR detector system will simultaneously measure many experimental observables to study signatures of the QGP phase transition as well as the space-time evolution of the collision process over a variety of colliding nuclear systems. In addition, STAR will investigate very peripheral collisions of relativistic nuclei to study photon and pomeron interactions resulting from the intense electromagnetic fields of the colliding ions and color-

less strong interactions, respectively.¹¹³ STAR will also have an active program of spin physics studies of the interactions of polarized protons at RHIC.¹¹¹

The STAR physics program is outlined schematically in Tables 1 and 2. The three primary categories of physics in STAR (relativistic heavy ion, polarized proton, and photon/pomeron) are listed. The relativistic heavy ion program is depicted as a function of time during the collision process, with initial collision impact listed at the top and time proceeding downward. Time starts with the initial state of the two incident nuclei. The various stages are underlined, the physics observables are listed on the left, and the quantities measured in STAR are listed in the column on the right. The relativistic heavy ion physics program of STAR will be presented for the various stages of the collision, and then the peripheral collision (photon/pomeron) physics program will be described.

Initial Conditions - Colliding Nuclei

The initial conditions will be studied in order to understand the structure functions of the quarks and gluons of the colliding nuclei. This will require 1) measurement of the nuclear structure functions of quarks and gluons in proton-proton interactions at RHIC energies, and 2) measurement of the structure functions of quarks and gluons in proton-nucleus interactions to determine the degree of nuclear shadowing of quarks and gluons at RHIC energies. Each of these studies will involve measurements of the elementary Compton process (gluon + quark $\rightarrow \gamma$ + quark jet) and other jet production processes. This will determine the initial flux of quarks and gluons within the incident nuclei. Such determinations are necessary as input to calculations of the production yields of various processes.

Early Gluon-Dominated Stage

Once a RHIC collision begins, hard scattering of quarks and gluons dominates the collision process.⁷ This stage is dominated by gluon interactions due to the shorter mean-free path of gluons as compared to quarks and due to the predominance of gluon producing reactions over quark producing ones. It is predicted that a gluon-dominated plasma forms.¹¹⁴

It is important to determine the characteristics of this early stage of the collision at RHIC. Since hard processes will dominate this stage of the collision, measurements of products of the hard scattering are necessary. STAR will measure high transverse momentum (p_{\perp}) photons, charged particles and jets. In addition, STAR is investigating ways of performing an open charm measurement via the hadronic or semi-leptonic channels of the decays of D-mesons.

STAR Physics at RHIC

A. RELATIVISTIC HEAVY ION COLLISIONS (* denotes event-by-event measurement capability)

STAR MEASUREMENTS

Initial Conditions

Nuclear structure functions / nuclear shadowing
(quark and gluon) γ -jet
jets

Early Gluon-dominated Plasma

Temperature (radiation) (Open Charm?), γ 's

Quark Gluon Plasma Transition and Mixed Phase

Thermalization $d^3\sigma/dp_t d\eta d\phi$ *
 Flavor equilibrium strangeness ($K^{\pm 0}$, Λ , Ξ , Ω) *
 Deconfinement (J/ψ suppression)
 Order of phase transition T, entropy, HBT
 Fluctuations $d^2E/d\eta d\phi$ *, $d^3\sigma/dp_t d\eta d\phi$ *
 Space-time evolution $\pi\pi^*$, $KK^{\pm 0}$ - HBT
 Mini-jet and jet propagation/attenuation high p_t particles
 γ -jet, * jets, * high p_t π^0

Chiral Symmetry Restoration

Resonance widths, masses, branching ratios $\phi \rightarrow KK$, (e^+e^-)
 Disoriented chiral condensates $E_t(\text{neutral}) / n(\text{charged})^*$
 π^{+-} spectra at low p_t

Hadronization Transition

Freeze-out conditions HBT*, T *
 Strangeness Distillation K^+ , K^- *

Collision Dynamics

Stopping and baryo-chemical potential $d^3\sigma/dp_t d\eta d\phi$ *
 Expansion dynamics (long./transverse flow) flow, $d^3\sigma/dp_t d\eta d\phi$
 $d^2E/d\eta d\phi$

Table 1: Schematic representation of the relativistic heavy ion physics component of the STAR physics program. The table is time-ordered as a function of the stage being probed of the collision process. Time starts with the initial states of the incident nuclei at the top and proceeds downward. The physics observables are listed on the left and the quantities measured in STAR are listed on the right. The two remaining categories of physics in STAR (polarized proton, and photon/pomeron physics) are listed in Table 2.

STAR Physics at RHIC (continued)

B. POLARIZED PROTON-PROTON INTERACTIONS

Spin Physics

Spin-dependent parton distributions

jet-jet, γ -jet, γ ,
 W^\pm , Z^0

C. PERIPHERAL COLLISIONS OF RELATIVISTIC HEAVY IONS (PHOTON/POMERON PHYSICS)

Peripheral Collision Physics ($\gamma\gamma$, γg , pomerons)

$f_2(1270)$, $f_0(975)$, $\rho^0\rho^0$, $\gamma g \rightarrow c\bar{c}$, pomeron int's

resonance decays
 $\pi^+\pi^-$
 $\pi^+\pi^-\pi^+\pi^-$, etc.

Table 2: Continuation of schematic representation of the STAR physics program (relativistic heavy ion, polarized proton, and photon/pomeron). Schematized in this table are the polarized proton, and photon/pomeron physics programs in STAR. The physics observables are listed on the left and the quantities measured in STAR are listed on the right.

At present, no techniques have been found to accomplish these measurements in STAR, without the addition of new detectors. Since a measurement of the charm production cross section is essential to be able to determine the charm contribution to the background for charmonium production, and thus understand the suppression of charmonium states and possible formation of a deconfined phase in relativistic heavy ion collisions, investigations into the possibility of measuring open charm in STAR continues.

Quark Gluon Plasma Transition and Mixed Phase

Strangeness and Particle Yields.

To determine the degree of equilibration of the system and to investigate fluctuations, STAR will measure triple differential cross sections for production of various types of particles as a function of transverse momentum (p_\perp), pseudo-rapidity (η) and azimuthal angle (ϕ). Since the hadrons that are measured in the final state are formed in the hadronization process after a possible QGP phase, the final state spectra of hadrons are a product of the various stages of evolution of the system. For a QGP to have formed, the yields of produced particles must be representative of a system in equilibrium at a temperature and baryo-chemical potential regime beyond that sustainable in hadronic matter (see Fig.1). To ascertain information on the high density phase, strange hadrons (K^+ , K^- , K^0) and singly- and multiply-strange

baryons ($\bar{\Lambda}$, Λ , Ξ^- , $\bar{\Xi}^+$, Ω) will be measured in STAR over a wide rapidity interval about mid-rapidity.¹¹⁵ These measurements will be used to determine the degree of saturation of the strangeness degree of freedom. An enhancement in the production of strange particles resulting from chemical equilibrium of a system of quarks and gluons was one of the first predictions for a signature of QGP formation.³⁴ From the measurements and ratios of strange particles and other hadrons, the baryo-chemical potential, temperature and degree of saturation in strangeness can be determined for various ensembles of events (impact parameter selections) and colliding systems in STAR. Coupled with theoretical predictions, this information can be used to determine whether a QGP has been formed. Some strangeness observations that are anticipated to accompany the formation of a QGP are an enhancement in the strange antibaryon content^{35,36} and an increased sensitivity of multiply-strange baryons (Ξ^- , $\bar{\Xi}^+$, Ω) compared to singly-strange hadrons³⁵ for the presence of a QGP.

Parton Propagation and Attenuation.

The products of hard scattering processes in the early stages of a relativistic heavy ion collision must traverse distances of several fermi through highly excited matter. The energy loss of these propagating quarks and gluons is predicted¹¹⁶ to be sensitive to the medium through which they travel, and may be a direct method of observing the excitation of the medium. As a result the spectra of high p_\perp particles and jets will be modified due to attenuation in the medium. The resulting spectra will represent the energy-loss history of the hard-scattered parton as it traverses the medium. If there is a large difference in the energy loss between highly excited hadronic matter and the QGP, then this quenching effect should be visible in the high p_\perp spectra of particles and jets. A systematic study of pp, p-nucleus and nucleus-nucleus collisions will be necessary to unravel the degree to which shadowing and quenching contribute to the particle spectra.

Hanbury-Brown and Twiss (HBT) Interferometry.

Correlations between identical bosons provide information on the freeze-out geometry, the expansion dynamics and possibly the existence of a QGP.¹¹⁷ STAR will measure the parameters of the pion-emitting source via pion correlation analysis on an event-by-event basis and will correlate them with other event observables. Moreover, the correlations of like-sign charged kaons or pions will be measured on an inclusive basis to high accuracy. The dependence of the source parameters on the transverse momentum components of the particle pairs will be measured with high statistics. Measurement of correlations between unlike-sign pairs will provide information for Coulomb corrections and

on effects of final state interactions. The KK correlation is less affected by resonance decays after hadronic freeze-out than the $\pi\pi$ correlations. The K's are expected to freeze out earlier¹¹⁸ than π 's in the expansion. Depending upon the baryo-chemical potential and the existence of a QGP, the K^+ and K^- freeze out at different times.

By reconstructing the decay topologies of $K_s^0 \rightarrow \pi^+\pi^-$, STAR will measure $K_s^0 K_s^0$ correlations.¹¹² In this case the absence of Coulomb repulsion, as compared to like-sign charged particle correlations, will enable a more precise measurement of the large source dimensions expected at RHIC. Since the K_s^0 is not a strangeness eigenstate, the $K_s^0 K_s^0$ correlations will contain an interference term which should provide additional space-time information and exhibit strangeness distillation effects in regions where the baryochemical potential is significant.¹¹⁹

Fluctuations in Energy, Entropy, Multiplicity and p_\perp .

It has long been known that a general indicator of a phase transition is the appearance of critical dynamical fluctuations in a narrow range of conditions. Such critical fluctuations can only be seen in individual events where the statistics are large enough to overcome uncertainties due to finite particle number fluctuations. The large transverse energy and multiplicity densities at midrapidity in central collisions allow event-by-event measurement of fluctuations in particle ratios, energy density, entropy density and flow of different types of particles as a function of p_\perp , rapidity, and azimuthal angle. Fluctuations have been predicted to arise from the process of hadronization of a QGP.¹²⁰

Chiral Symmetry Restoration

Resonance Widths, Masses, Branching Ratios.

The production cross section of ϕ -mesons will be measured inclusively in STAR via the decay $\phi \rightarrow K^+K^-$. Measurement of the yield of the ϕ , which is an $s\bar{s}$ pair, places a more stringent constraint on the origin of the observed flavor composition¹²¹ than the K/π ratio and is expected to be more sensitive to the presence of a QGP. The ϕ mass, width and production rate are also expected to be extremely sensitive to changes in the quark masses¹²² due to a possible chiral phase transition at high energy densities. STAR will measure $\phi \rightarrow K^+K^-$ and with lower statistics $\phi \rightarrow e^+e^-$ in order to determine the yield, mass, and width of the ϕ produced in central collisions at RHIC.

Electromagnetic/Charged Particle Energy Ratio.

The measurement of EM energy vs. charged-particle energy is an impor-

tant correlation to measure in STAR in the search for the QGP and other new physics. The imbalance between charged particle and neutral energy observed in Centauro and other cosmic ray events emphasizes the need for EM/charged particle measurements.¹²³ Such abnormal ratios of neutral to charged-particle energy and multiplicity have been associated with the formation of disoriented chiral condensates.¹²⁴

Spectra at Low p_{\perp} .

Using the silicon vertex tracking, STAR will measure the spectra of charged pions at low p_{\perp} in order to investigate effects of the presence of a disoriented chiral condensate. A summary of STAR's capabilities and the sensitivities to parameters of the DCC domain size can be found in Ref. 125.

Hadronization Transition

Freeze-Out Conditions.

Both two-particle interferometry (discussed above) and single particle inclusive transverse momentum distributions provide information on the freeze-out geometry and the expansion dynamics of the collision. As a consequence of the high multiplicities in central collision events, the slope of the transverse momentum (p_{\perp}) distribution for pions and the $\langle p_{\perp} \rangle$ for pions and kaons can be determined event-by-event in STAR. Thus, individual events can be characterized by a pion slope parameter T_o (effective "temperature") or $\langle p_{\perp} \rangle$, and a kaon $\langle p_{\perp} \rangle$ in order to search for events with extremely high temperature, predicted¹²⁶ to result from deflagration of a QGP. The determination of $\langle p_{\perp} \rangle$ for pions can be made very accurately on the single event basis in this experiment, over the expected range of multiplicities in central collisions from Ca + Ca to Au + Au. For kaons, with ~ 200 charged kaons per event in the acceptance for central Au + Au events, $\langle p_{\perp} \rangle$ can also be determined accurately for single events.

Strangeness Distillation.

The spectra of K^+ and K^- will be measured accurately in STAR and compared for regions of different baryo-chemical potential in order to determine if effects of strangeness distillation are present. Such distillation effects are predicted to occur in the presence of a QGP.¹¹⁹

Expansion Dynamics, Stopping, Baryo-Chemical Potential.

Inclusive p_{\perp} distributions of charged particles will be measured with high statistics in STAR to investigate various effects. These include collective radial

flow and critical temperature at low p_{\perp} , and mini-jet attenuation¹²⁷ at high p_{\perp} . The p_{\perp} spectra of baryons and anti-baryons at midrapidity are particularly interesting for determining the stopping power of quarks. Measurements of the net baryon number and net charge are important for establishing the baryochemical potential at midrapidity.

Peripheral Collision (Photon/Pomeron) Physics

Nuclei colliding at ultra-relativistic velocities produce intense electromagnetic fields, which can act as a coherent source of photons for the study of $\gamma\gamma$ interactions. Likewise, the colorless strong force fields of the interacting nuclei can act as a coherent source of pomerons. These allow the possibility of also studying γ -pomeron and pomeron-pomeron interactions by investigating the possible final state couplings and hadronic final states resulting from collisions of relativistic heavy ions. Since the photon flux will be enhanced by a factor of the square of the nuclear charge, the high photon-photon luminosities at RHIC will allow a thorough study of many vector meson final states in the 1 to 2 GeV mass range. This is of particular interest since the results of e^+e^- and proton-proton interaction experiments have exhibited many more particles in this mass range than fits comfortably into SU(3). STAR will measure charged-particle exclusive final states with few particles in order to reconstruct the final state of the interaction. Peripheral collisions will be studied to decrease the background of particles from nuclear interactions. The initial program in STAR will involve a study of $\gamma\gamma \rightarrow e^+e^-$ and $\gamma\gamma \rightarrow \mu^+\mu^-$ to measure the incident flux for $\gamma\gamma$ interactions. Then various final states, e.g. $f_2(1270)$ or $\rho^0\rho^0$, will be measured and compared to their expected couplings to the two-photon incident state. This will lead to an investigation of more exotic states that have been seen in e^+e^- and proton-proton interactions, e.g. candidates for multi-quark(gluon) and/or mixed states. Thus, additional information can be learned about these exotic states based upon their anticipated couplings to two-photons. In addition, vector meson states formed in γ -pomeron interactions will be studied. More detailed information on this program in STAR can be found in Ref. 113.

3.2 The PHENIX Experiment

The physics goals of PHENIX (Pioneering High Energy Nuclear Interaction eXperiment)¹²⁸ are to measure as many potential signatures of the QGP as possible as a function of a well-defined common variable such as impact parameter or pseudorapidity density. PHENIX will measure lepton pairs (di-electrons and di-muons), photons and hadrons. The experiment will be sensi-

PHENIX Detector

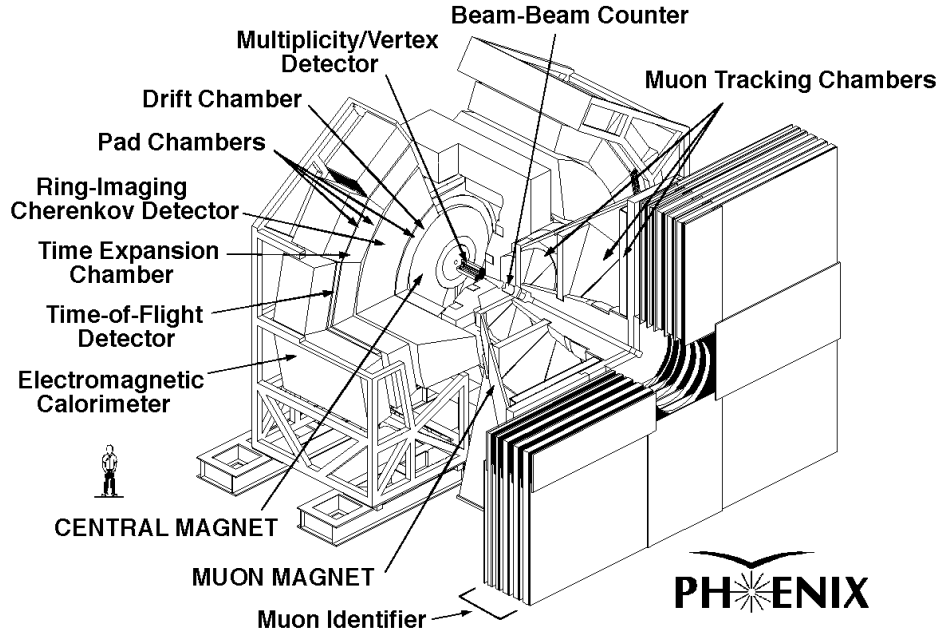


Figure 14: A diagram of the PHENIX experiment at RHIC. The beams collide along the horizontal direction in the center of the detector. The detector components are defined in the text.

tive to very small cross section processes such as the production of the J/ψ , ψ' , Υ and high p_{\perp} spectra. It will also have the capability for high rates with pp and pA collisions. A diagram of the PHENIX detector system is displayed in Fig.14. The magnet has an axial field along the beam direction with tracking chambers and detectors for the identification of electrons, muons, photons and hadrons installed outside the field. There are two arms for dielectron measurements, each with 1 steradian acceptance at midrapidity. Each arm is equipped with a ring-imaging Cerenkov detector (RICH), a time-expansion chamber (TEC) for dE/dx measurements, time-of-flight detectors (TOF), and an electromagnetic calorimeter (EM Cal). Photons and hadrons will also be measured at midrapidity with 2 and 0.36 steradian acceptances, respectively.

Separate muon spectrometers with 1 steradian acceptance each are located at forward rapidities as shown in Fig.14. The magnetic field in each muon arm is transverse to the beam direction. A silicon multiplicity-vertex detector (MVD) and beam-beam coincidence counters are located near the interaction vertex. The MVD covers $|\eta| < 2.7$ about midrapidity for event selection via charged-particle multiplicity.

PHENIX will investigate the degree of deconfinement in RHIC collisions, and thus the possibility of QGP formation, by measuring the yields of J/ψ , ψ' , Υ . If the J/ψ radius is larger than the Debye screening length then the QCD potential between the $c\bar{c}$ pairs, which form a J/ψ , is weakened and J/ψ formation suppressed.³⁰ Since the J/ψ , ψ' , Υ binding and thus their radii are different, i.e. $r(\psi') > r(J/\psi) > r(\Upsilon)$, a study of the relative suppression of these is sensitive to the screening in a QGP and will help differentiate between deconfinement and possible dissociation in hot nuclear matter. PHENIX will measure J/ψ via electron-pairs near midrapidity and J/ψ , ψ' , Υ via muon-pairs at forward angles. The anticipated raw muon-pair mass spectrum in the forward muon arm is displayed in Fig.15 for one-month of RHIC operation at the design luminosity for central Au + Au collisions. Peaks for the J/ψ , ψ' and Υ can be observed. With subtraction of like-sign muon-pairs, and application of kinematic cuts the peak-to-background of this spectrum is expected to improve further and the ψ' peak will become more prominent. For one year of running at the RHIC design luminosity of $2 \times 10^{26} \text{ cm}^{-2}\text{s}^{-1}$, PHENIX will detect 390K J/ψ , 5.7K ψ' and 1.2K Υ for central collisions (top 10 % in centrality) of Au + Au. The mass resolution is about 100 MeV for the J/ψ and the pion rejection is somewhat better than 10^{-4} at $p > 2.5 \text{ GeV}/c$. In addition to these charmonium studies, PHENIX will measure open charm (D, \bar{D} decays) via unlike-sign $e\mu$ coincidences using the electron and muon spectrometers. The rate of open charm production is expected to be sensitive to details of the early stages of RHIC collisions and will provide complimentary information to the charmonium studies.

PHENIX will investigate possible chiral symmetry restoration by performing high resolution measurements of the leptonic and hadronic decays of ϕ -mesons. In a chirally-restored QGP both the ϕ -meson and kaon masses may be modified resulting in change in the mass and width of the ϕ -meson and the branching ratio between leptonic and hadronic channels.²⁴ The anticipated electron-pair spectrum for 8 days of central trigger Au + Au operation at RHIC is shown in Fig.16. Extremely sharp peaks for the ω , ϕ , and J/ψ are observed, with a 2-to-1 signal-to-noise ratio in the low mass resonance region. The mass resolution is approximately 4 MeV for the ϕ decaying to e^+e^- (and $\sim 1 \text{ MeV}$ for ϕ decaying to K^+K^- in the hadronic measurement). The pion

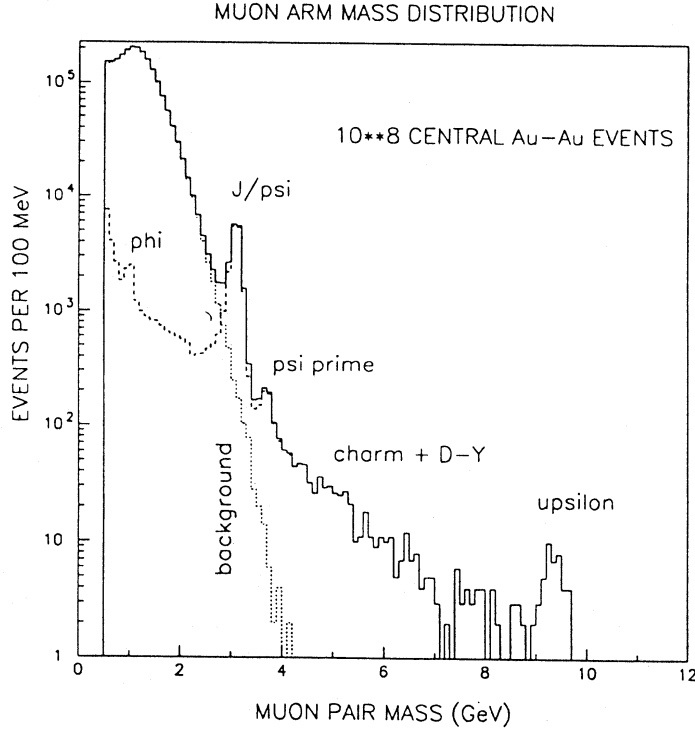


Figure 15: PHENIX muon-pair mass spectrum anticipated in one month of RHIC running for central Au + Au collisions at a luminosity of $2 \times 10^{26} \text{ cm}^{-2}\text{s}^{-1}$.

rejection is better than 10^{-4} for $p < 4 \text{ GeV}/c$.

There are various other measurements of interest that will be undertaken by PHENIX. Measurements will be made using the electromagnetic calorimeter to determine the yield of direct photons radiated from the nuclear interaction. An enhancement of photons with $p_{\perp} > 2$ to $3 \text{ GeV}/c$ is expected because of the high gluon concentration in the early high energy-density stage of RHIC collisions.¹²⁹ PHENIX will also investigate the order of the QGP phase transition by measuring the $\langle p_{\perp} \rangle$ of identified-charged pions, kaons and protons at mid-rapidity as a function of the energy density. By detecting both hadrons and photons, PHENIX can measure fluctuations in isospin, $\pi^0/(\pi^+ + \pi^-)$, which should occur if a DCC is formed.¹³⁰ PHENIX will also study strangeness and charm production for enhancements, jet-quenching, and the

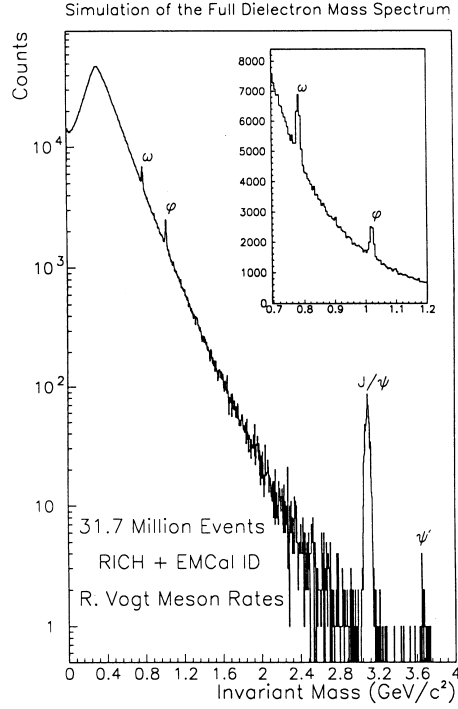


Figure 16: PHENIX electron-pair mass spectrum anticipated in 8 days of RHIC running for central Au + Au collisions at a luminosity of $2 \times 10^{26} \text{ cm}^{-2}\text{s}^{-1}$.

space-time evolution of the system as a function of energy density.

3.3 The PHOBOS Experiment

The physics goals of the PHOBOS experiment¹³¹ are to measure single particle spectra and correlations between particles with low transverse momenta and to characterize events using a multiplicity detector. Charged particles will be measured and identified in the range $0 < y < 1.5$ and $15 \text{ MeV}/c < p_{\perp} < 600 \text{ MeV}/c$ for pions and $45 \text{ MeV}/c < p_{\perp} < 1200 \text{ MeV}/c$ for protons. The range of particles to be studied include γ , π , K , ρ , $\bar{\rho}$, ϕ , Λ , $\bar{\Lambda}$, d , and \bar{d} . Particle ratios, p_{\perp} spectra, strangeness production (K , ϕ , Λ , $\bar{\Lambda}$) and particle correlations will be studied. An illustration of the experiment is shown in Fig.17. The top coils

and magnet iron are not shown in order to see the other components. The multiplicity detector consists of silicon strip detectors and silicon pad detectors. The two magnetic arms have a field strength of 2 Tesla. Eleven layers of silicon, 5 layers of pads and 6 layers of strips, are installed in each magnetic spectrometer for tracking and momentum measurements.

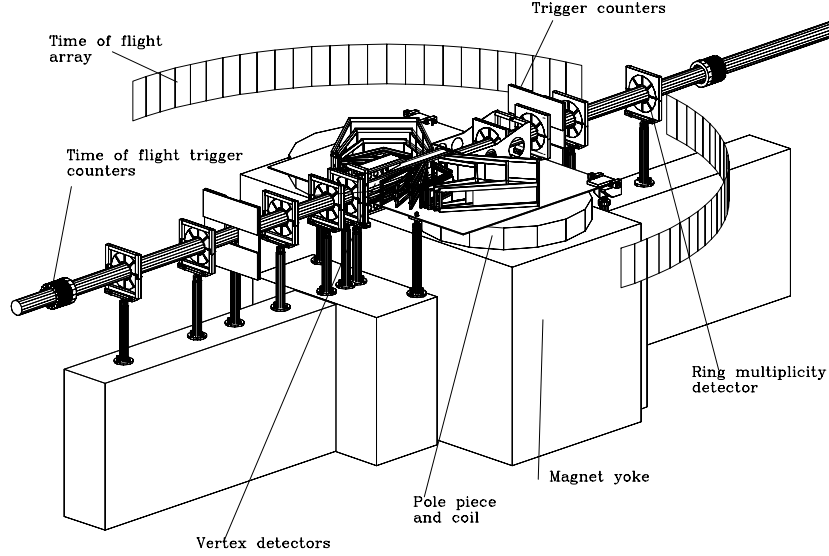


Figure 17: A diagram of the PHOBOS two-arm multiparticle spectrometer. The two arms are located on opposite sides of the beam pipe. Each arm has a 2 Tesla magnet represented by only the lower coils for ease of viewing other parts of the set-up, with silicon detector planes for tracking.

3.4 The BRAHMS Experiment

The physics goals of the BRAHMS (BRoad Range Hadron Magnetic Spectrometers) experiment¹³² are to achieve a basic understanding of relativistic heavy ion collisions at RHIC through a systematic study of particle production in AA collisions from the peripheral to the most central in impact parameter. Measurements will be performed using two high resolution magnetic spectrometers at various angles to cover both the baryon-rich fragmentation regions and the high temperature, baryon-depleted midrapidity region. A diagram of the

BRAHMS forward and midrapidity spectrometers is shown in Fig.18. The spectrometers will measure and identify inclusive and semi-inclusive π , K and p, and their momenta with high statistics over a small solid angle and over a wide range of pseudorapidity ($0 < \eta < 4$) and transverse momentum. Particle identification is performed using various combinations of time-of-flight arrays, and threshold and ring-imaging Cherenkov counters. BRAHMS will measure inclusive and semi-inclusive particle spectra, and extract the net baryon densities and temperatures from spectral slopes as a function of rapidity to determine whether thermal and chemical equilibrium are reached in these collisions. It will also be able to study both high and low transverse momentum processes. Centrality will be measured using a global multiplicity detector.

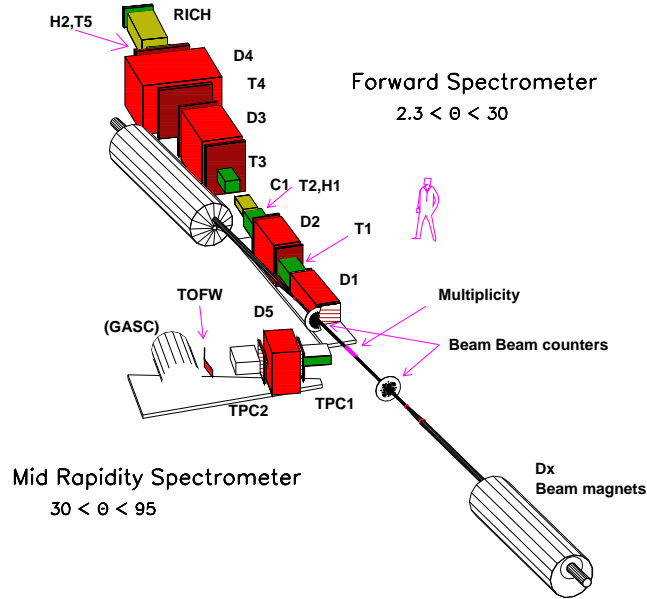


Figure 18: A diagram of the BRAHMS forward and midrapidity spectrometers in the narrow angle hall at RHIC.

3.5 Overview of Spin Physics at RHIC

The topic of the spin of the nucleon is the subject of another set of lectures at this Institute.¹³³ It will be discussed briefly here, in that another physics goal of RHIC is to make significant advances towards understanding

the spin of the proton. This issue has been pursued in deep inelastic scattering experiments at SLAC, CERN and now HERMES at DESY in order to determine the contributions of valence quarks and now the gluon to the proton's spin. The spin of the proton can be divided into contributions from quarks (Δq), gluons (ΔG) and orbital angular momentum (ΔL) and written as $S_{proton} = 0.5\Delta q + \Delta G + \Delta L = 1/2$. Though the valence quarks were initially thought to make up most, if not all, of the proton spin ($= 1/2$) it was found that this is not the case. The contribution from valence quarks has been measured and the world data presently place the value of $\Delta q = 0.30 \pm 0.10$. This has left considerable room for other contributions to the spin of the proton and in particular it will be necessary to go to higher energies to increase the accuracy of the value of the quark contribution to the proton spin. The contribution from gluons has yet to be measured and that of orbital angular momentum is probably unmeasurable, except by subtraction after all other contributions are known.

RHIC will provide the opportunity for the gluon component of the proton spin to be measured. This will be possible by colliding polarized protons at momenta up to 250 GeV/c each at RHIC, and measuring asymmetries for high p_{\perp} photons, Drell-Yan, jets, W^{\pm} , and Z^0 . At these energies one is in the perturbative QCD regime with high values of momentum transfer (Q^2) and cm energy, where quantities are calculable and QCD can be tested. As a polarized proton collider, RHIC is expected to attain luminosities of up to $2 \times 10^{32} cm^{-2} s^{-1}$, with a polarization of 70%, and is anticipated to operate in this mode for an average of 10 weeks per year. At present both large experiments, STAR and PHENIX, have spin physics programs approved at RHIC.

There are also other experiments around the world which have been proposed to undertake measurements of the polarized gluon structure function. The COMPASS experiment¹³⁴ has been proposed to utilize a polarized muon beam at CERN impinging on a polarized (proton) target. This experiment would concentrate on measuring the production of open charm to determine the polarized gluon structure function. Farther in the future could be a polarized electron-proton collider at DESY. There are some first indications from existing polarized fixed-target experiments that the gluon contributions at low x are large.¹³³

A summary of the spin asymmetry measurements at RHIC follows. The gluon spin structure function $\Delta G(x)$, where x is the fraction of the proton momentum carried by the parton, can be determined by measuring the asymmetries for the production of photons, jets and photon-jet coincidences. The measured double spin asymmetry is defined as $A_{LL} = (d\sigma^{++} - d\sigma^{+-})/(d\sigma^{++} +$

$d\sigma^{+-}$), where $d\sigma^{++}$ corresponds to the case where the longitudinal polarization of the two proton beams are aligned and $d\sigma^{+-}$ to the anti-aligned case. Since the polarized proton beams appear as beams of polarized partons, the asymmetry A_{LL} can be measured for a given process and then related to the polarized structure function at the parton level.¹³³

Measuring the asymmetry for production of direct photons, which result from the $qg \rightarrow q\gamma$ Compton process, as a function of x provides a measurement of the polarized gluon structure function from the parton level equation $A_{LL} = a_{LL}(qg \rightarrow \gamma q)(\Delta q(x)/q(x))(\Delta G(x)/G(x))$. Here $\Delta q(x)/q(x)$ for the valence quarks is taken from deep inelastic scattering measurements, and $a_{LL}(qg \rightarrow \gamma q)$ is the elementary parton level process which is calculable in perturbative QCD. Another process which contributes to asymmetries in the direct photon production is the annihilation process $q\bar{q} \rightarrow g\gamma$, although this contribution is rather small since there are much fewer anti-quarks than quarks in the proton beams. All relevant processes must also be folded into analysis of the measured double spin asymmetry for production of direct photons.¹³⁵ Similarly, the double spin asymmetry can be measured in jet production and in γ -jet coincidences as a function of p_{\perp} .

The contribution of sea quarks to the spin of the proton can be measured in polarized proton-proton collisions at RHIC. The Drell-Yan process (involving $q\bar{q}$) provides a measure of the asymmetry for $\Delta\bar{q}$, W^+ (involving $d\bar{u}$) measurements for $\Delta\bar{u}$, and W^- (involving $u\bar{d}$) measurements for $\Delta\bar{d}$. In addition, both parity-conserving and parity-violating asymmetries of W^{\pm} production can be measured to provide tests of fundamental symmetries in QCD.¹³⁶

Another fundamental structure function which can only be measured in polarized proton-proton collisions is the transversity Δh_1 .¹³⁷ This structure function involves the correlation between left- and right-handed quarks in a transversely polarized proton beam. It is not observable in deep inelastic scattering on a single quark, and requires double transverse spin asymmetry measurements for Drell-Yan and Z^0 production.

It is clear that in addition to the relativistic heavy ion program for which RHIC was constructed, there will also be a broad program of fundamental spin structure function measurements at RHIC.

Acknowledgments

The author apologizes to those whose data are not included in this overview, and thanks Brant Johnson for providing some of the figures, Brian Lasiuk and Thomas Ullrich for general assistance, and Jennifer Tenedine for assistance with the manuscript. This work was supported in part by the Director, Office

of Energy Research, Division of Nuclear Physics of the Office of High Energy and Nuclear Physics of the U.S. Department of Energy under contract No. DE-FG02-91ER-40609.

References

1. J.C. Collins and M.J. Perry, *Phys. Rev. Lett.* **34**, 1353 (1975); G. Chapline and L. Susskind, *Phys. Rev. D* **20**, 2610 (1979).
2. Conceptual Design of the Relativistic Heavy Ion Collider, Report BNL 52195 (1989).
3. T.D. Lee and G.C. Wick, *Phys. Rev. D* **9**, 2291 (1974); T.D. Lee, *Rev. Mod. Phys.* **47**, 267 (1975).
4. for a review see M. Schmelling, Proceedings of the XXVIII International Conference on High Energy Physics, Warsaw (1996).
5. T. Blum et al, *Phys. Rev. D* **51**, 5153 (1995).
6. G.C. Blazey, Intersections between Particle and Nuclear Physics, 6th Conference, ed. T.W. Donnelly, AIP Press, p. 18 (1997).
7. K. Geiger and B. Mueller, *Nucl. Phys. B* **369**, 600 (1992).
8. S.A. Bass et al, preprint nucl-th/9803035 (1998).
9. L. van Hove, *Phys. Lett. B* **118**, 138 (1982); *Z. Phys. C* **21**, 93 (1983).
10. P.V. Ruuskanen, *Nucl. Phys. A* **525**, 255c (1991); *ibid.* **A 544**, 169c (1992).
11. K. Geiger and J.I. Kapusta, *Phys. Rev. Lett.* **70**, 1920 (1993).
12. M.T. Strickland, *Phys. Lett. B* **331**, 245 (1994).
13. C. Gale and J. Kapusta, *Phys. Rev. C* **35**, 2107 (1987).
14. F. Karsch, K. Redlich, and L. Turko, *Z. Phys. C* **60**, 519 (1995).
15. R.D. Pisarski, *Phys. Lett. B* **110**, 155 (1982).
16. A.I. Bohkarev and M.E. Shaposhnikov, *Phys. Lett. B* **145**, 276 (1984); *Nucl. Phys. B* **268**, 220 (1986); *Z. Phys. C* **36**, 267 (1987).
17. H.G. Dosch and S. Narison, *Phys. Lett. B* **203**, 155 (1988).
18. R.J. Furnstahl, T. Hatsuda and S.H. Lee, *Phys. Rev. D* **42**, 1744 (1990).
19. C. Gale and J. Kapusta, *Nucl. Phys. B* **357**, 65 (1991).
20. Z. Aouissat, G. Chanfray, P. Schuck and G. Welke, *Z. Phys. A* **340**, 347 (1991).
21. M. Asakawa, C.M. Ko, P. Lévai and W.J. Qiu, *Phys. Rev. C* **46**, 1159 (1992).
22. M. Herrmann, B.L. Friman and W. Nörenberg, *Z. Phys. A* **343**, 119 (1992).
23. T. Hatsuda, Y. Koike and S.H. Lee, *Nucl. Phys. B* **394**, 221 (1993).
24. D. Lissauer and E.V. Shuryak, *Phys. Lett. B* **253**, 15 (1991).

25. P.Z. Bi and J. Rafelski, *Phys. Lett. B* **262**, 485 (1991).
26. M. Asakawa and C.M. Ko, *Phys. Lett. B* **322**, 33 (1994); C.M. Ko and D. Seibert, *Phys. Rev. C* **49**, 2198 (1994).
27. U. Heinz and K.S. Lee, *Phys. Lett. B* **259**, 162 (1991).
28. D.K. Srivastava, B. Sinha, M. Gyulassy and X.N. Wang, *Phys. Lett. B* **276**, 285 (1992).
29. S. Chakrabarty, J. Alam, S. Raha, B. Sinha and K. Srivastava, *Phys. Rev. D* **46**, 3802 (1992).
30. T. Matsui and H. Satz, *Phys. Lett. B* **178**, 416 (1986).
31. F. Karsch, M.T. Mehr and H. Satz, *Z. Phys. C* **37**, 617 (1988).
32. F. Karsch and H. Satz, *Z. Phys. C* **51**, 209 (1991).
33. J.P. Bailly et al, *Phys. Lett. B* **195**, 609 (1987).
34. J. Rafelski and B. Müller, *Phys. Rev. Lett.* **48**, 1066 (1982). [Erratum: *ibid.* **56**, 2334 (1986).]
35. J. Rafelski, *Phys. Rep.* **88**, 331 (1982).
36. P. Koch, B. Müller and J. Rafelski, *Phys. Rep.* **142**, 167 (1986).
37. H.W. Barz, G.L. Friman, J. Knoll and H. Schulz, *Nucl. Phys. A* **484**, 661 (1988); *Nucl. Phys. A* **519**, 831 (1990); *Phys. Lett. B* **254**, 315 (1991).
38. J.D. Bjorken, *Acta Phys. Polon. B* **23**, 637 (1992).
39. C.M.G. Lattes, Y. Fujimoto and S. Hasegawa, *Phys. Rep.* **65**, 151 (1980).
40. C.S. Lam and S.Y. Lo, *Phys. Rev. Lett.* **52**, 1184 (1984); *Phys. Rev. D* **33**, 1336 (1986).
41. S. Pratt, *Phys. Lett. B* **301**, 159 (1993); S. Pratt and V. Zelevinsky, *Phys. Rev. Lett.* **72**, 816 (1994).
42. C. Greiner, C. Gong and B. Müller, *Phys. Lett. B* **316**, 226 (1993).
43. T.A. DeGrand, *Phys. Rev. D* **30**, 2001 (1984).
44. J. Ellis, U. Heinz and K.L. Kowalski, *Phys. Lett. B* **233**, 223 (1989).
45. J.I. Kapusta and A. Srivastava, *Phys. Rev. D* **50**, 5379 (1994).
46. J.D. Bjorken, Fermilab publication 82/59, Batavia (1982), unpublished.
47. B. Svetitsky, *Phys. Rev. D* **37**, 2484 (1988).
48. M.H. Thoma and M. Gyulassy, *Nucl. Phys. B* **351**, 491 (1991); E. Braaten and M.H. Thoma, *Phys. Rev. D* **44**, R2625 (1991).
49. S. Mrówczyński, *Phys. Lett. B* **269**, 383 (1991).
50. Y. Koike and T. Matsui, *Phys. Rev. D* **45**, 3237 (1992).
51. A.B. Migdal, *Sov. Phys. JETP* **5**, 527 (1957).
52. M. Gyulassy and X.N. Wang, *Nucl. Phys. B* **420**, 583 (1994).
53. R. Baier, Y.L. Dokshitzer, S. Peigné and D. Schiff, *Phys. Lett. B* **345**, 277 (1995).
54. D.A. Appel, *Phys. Rev. D* **33**, 717 (1986).

55. J.P. Blaizot and L. McLerran, *Phys. Rev. D* **34**, 2739 (1986).
56. J. Pan and C. Gale, *Phys. Rev. D* **50**, 3235 (1994).
57. M.D. Corcoran et al, *Phys. Lett. B* **259**, 209 (1991).
58. J. Barrette et al, *Phys. Rev. Lett.* **70**, 299 (1993).
59. T. Alber et al, *Phys. Rev. Lett.* **75**, 3814 (1995).
60. J.D. Bjorken, *Phys. Rev. D* **27**, 140 (1983).
61. E. Laerman, *Nucl. Phys. A* **610**, 1c (1996).
62. G. Roland et al, Proceedings of the Thirteenth International Conference on Ultra-Relativistic Nucleus-Nucleus Collisions - Quark Matter '97, to be published in *Nucl. Phys. A* (1998).
63. J. Baechler et al, *Phys. Rev. Lett.* **72**, 1419 (1994).
64. J. Dodd, et al, Proc. of the XXV International Symposium on Multiparticle Dynamics, Stara Lesnia, Slovakia (1995); N. Xu et al, *Nucl. Phys. A* **610**, 175c (1996).
65. T. Abbott et al, *Phys. Rev. C* **50**, 1024 (1994).
66. L. Ahle et al, *Nucl. Phys. A* **610**, 139c (1996).
67. J. Barrette et al, *Phys. Rev. C* **50**, 3047 (1994).
68. J. Barrette et al, *Nucl. Phys. A* **610**, 153c (1996).
69. P. Jones et al, *Nucl. Phys. A* **610**, 188c (1996).
70. N. Xu et al, *Nucl. Phys. A* **610**, 175c (1996).
71. S. Ahmad et al, *Phys. Lett. B* **382**, 35 (1996).
72. H. Boggild et al, *Phys. Lett. B* **372**, 339 (1996); I.G. Bearden et al., *Phys. Rev. Lett.* **78**, 2080 (1997).
73. A. Sakaguchi et al, Proceedings of the Thirteenth International Conference on Ultra-Relativistic Nucleus-Nucleus Collisions - Quark Matter '97, to be published in *Nucl. Phys. A* (1998).
74. J. Sollfrank et al, *Z. Phys. C* **52**, 593 (1991); E. Schnedermann et al, *Phys. Rev. C* **48**, 2462 (1993).
75. U. Heinz, *Nucl. Phys. A* **610**, 264c (1996).
76. see papers in section on flow in *Nucl. Phys. A* **610**, (1996)
77. H. Appelshaeuser et al, *Phys. Rev. Lett.* **80**, 4136 (1998).
78. for a review of the theoretical approach see S. Pratt, Proceedings of the Thirteenth International Conference on Ultra-Relativistic Nucleus-Nucleus Collisions - Quark Matter '97, to be published in *Nucl. Phys. A* (1998).
79. H. Sorge, *Phys. Rev. Lett.* **78**, 2309 (1997).
80. J. Stachel, *Nucl Phys. A* **610**, 509c (1996).
81. P. Braun-Munzinger et al, *Phys. Lett. B* **365**, 1 (1996).
82. F. Becattini et al, preprint hep-ph/9710529 (1997).

83. F. Becattini, Proceedings of the Thirteenth International Conference on Ultra-Relativistic Nucleus-Nucleus Collisions - Quark Matter '97, to be published in *Nucl. Phys. A* (1998).
84. P. Braun-Munzinger, Proceedings of the Thirteenth International Conference on Ultra-Relativistic Nucleus-Nucleus Collisions - Quark Matter '97, to be published in *Nucl. Phys. A* (1998).
85. M. Kaneta et al, Proceedings of the Thirteenth International Conference on Ultra-Relativistic Nucleus-Nucleus Collisions - Quark Matter '97, to be published in *Nucl. Phys. A* (1998).
86. Proceedings of the Twelfth International Conference on Ultra-Relativistic Nucleus-Nucleus Collisions - Quark Matter '96, *Nucl. Phys. A* **610**, 1c (1996).
87. Proceedings of the Thirteenth International Conference on Ultra-Relativistic Nucleus-Nucleus Collisions - Quark Matter '97, to be published in *Nucl. Phys. A* (1998).
88. L. Ramello et al, Proceedings of the Thirteenth International Conference on Ultra-Relativistic Nucleus-Nucleus Collisions - Quark Matter '97, to be published in *Nucl. Phys. A* (1998).
89. C. Baglin et al, *Phys. Lett. B* **220**, 471 (1989); *ibid. B* **255**, 459 (1991); *ibid. B* **270**, 105 (1991).
90. M.C. Abreu et al, *Phys. Lett. B* **410**, 327 (1997); *ibid. Phys. Lett. B* **410**, 337 (1997).
91. see for example D. Kharzeev and H. Satz, *Phys. Lett. B* **366**, 316 (1996).
92. S. Gavin and R. Vogt, *Nucl. Phys. A* **61**, 442c (1996); S. Gavin et al., preprint hep-ph/9610432.
93. A. Capella et al, *Phys. Lett. B* **393**, 431 (1997).
94. W. Cassing and C.M. Ko, *Phys. Lett. B* **396**, 39 (1997).
95. D. Kharzeev et al, preprint BI-TP 97/02.
96. I. Ravinovich et al, Proceedings of the Thirteenth International Conference on Ultra-Relativistic Nucleus-Nucleus Collisions - Quark Matter '97, to be published in *Nucl. Phys. A* (1998).
97. G. Agakichiev et al, *Phys. Rev. Lett.* **75**, 1272 (1995); *ibid. Nucl. Phys. A* **610**, 317c (1996).
98. see relevant papers in *Nucl. Phys. A* **610**, (1996).
99. G.Q. Lee, C.M. Ko, and G.E. Brown, *Phys. Rev. Lett.* **75**, 4007 (1995); *ibid. Nucl. Phys. A* **606**, 568 (1996); G.Q. Lee et al, *Nucl. Phys. A* **611**, 539 (1996).
100. G.E. Brown and M. Rho, *Phys. Rev. Lett.* **66**, 2720 (1991).
101. T. Hatsuda and S.H. Lee, *Phys. Rev. C* **46**, R34 (1992).
102. M. Masera et al, *Nucl. Phys. A* **590**, 127c (1995).

103. J. Wambach, Proceedings of the Thirteenth International Conference on Ultra-Relativistic Nucleus-Nucleus Collisions - Quark Matter '97, to be published in *Nucl. Phys. A* (1998).
104. A. Falco et al, Proceedings of the Thirteenth International Conference on Ultra-Relativistic Nucleus-Nucleus Collisions - Quark Matter '97, to be published in *Nucl. Phys. A* (1998).
105. I. Tsurruya, Proceedings of the Thirteenth International Conference on Ultra-Relativistic Nucleus-Nucleus Collisions - Quark Matter '97, to be published in *Nucl. Phys. A* (1998).
106. G. Agakichiev et al, *Phys. Rev. Lett.* **75**, 1272 (1995).
107. T. Akesson et al, *Z. Phys. C* **46**, 369 (1990).
108. R. Albrecht et al, CERN PPE/95-186 (1995); T. Peitzmann et al, *Nucl. Phys. A* **610**, 200c (1996).
109. M.M. Aggarwal et al, Proceedings of the Thirteenth International Conference on Ultra-Relativistic Nucleus-Nucleus Collisions - Quark Matter '97, to be published in *Nucl. Phys. A* (1998).
110. X.N. Wang preprint hep-ph/9804357 (1998).
111. Proposal on Spin Physics Using the RHIC Polarized Collider, RHIC Spin Collaboration (1992).
112. Conceptual Design Report for the Solenoidal Tracker At RHIC, The STAR Collaboration, PUB-5347 (1992); J.W. Harris et al, *Nucl. Phys. A* **566**, 277c (1994).
113. S. Klein and E. Scannapieco in *Proceedings on Intersections Between Particle and Nuclear Physics: 6th Conference*, ed. T.W. Donnelly (AIP Press, 1997), and LBNL Report LBNL-40495; J. Nystrand and S. Klein to be published in *Proceedings of Hadron '97*, and LBNL Report LBNL-41111 (1997).
114. E. Shuryak, *Phys. Rev. Lett.* **68**, 3270 (1992).
115. K. Wilson in *Proceedings of Quark Matter '95 Pre-conference Workshop*, ed. J. Thomas and T. Hallman, Report No. UCRL-ID-121571 (1995).
116. M. Gyulassy and M. Plummer, *Phys. Lett. B* **243**, 432 (1990); X.N. Wang and M. Gyulassy, *Phys. Rev. Lett.* **68**, 1480 (1992).
117. S. Pratt, *Phys. Rev. D* **33**, 1314 (1986); G. Bertsch, M. Gong and M. Tohyama, *Phys. Rev. C* **37**, 1896 (1988); and G. Bertsch, *Nucl. Phys. A* **498**, 151c (1989).
118. K.S. Lee, M.J. Rhoades-Brown and U. Heinz, *Phys. Rev. C* **37**, 1463 (1988).
119. M. Gyulassy, Lawrence Berkeley Laboratory Preprint LBL-32051 (1992).

120. M. Gyulassy, *Nucl. Phys. A* **400**, 31c (1983); L. van Hove, *Z. Phys. C* **27**, 135 (1985).
121. A. Shor, *Phys. Rev. Lett.* **54**, 1122 (1985).
122. R.D. Pisarski and F. Wilczek, *Phys. Rev. D* **29**, 338 (1984); T. Hatsuda and T. Kunihiro, *Phys. Lett. B* **185**, 304 (1987).
123. J.D. Bjorken and L.D. McLerran, *Phys. Rev. D* **20**, 2353 (1979); Y. Takahashi and S. Dake, *Nucl. Phys. A* **461**, 263c (1987).
124. J.D. Bjorken, *Int. J. Mod. Phys. A* **7**, 4189 (1992); K. Rajagopal and F. Wilczek, *Nucl. Phys. B* **404**, 577 (1993).
125. R. Bellwied in *Proceedings of Quark Matter '95 Pre-conference Workshop*, ed. J. Thomas and T. Hallman (Report No. UCRL-ID-121571, 1995).
126. E.V. Shuryak and O.V. Zhirov, *Phys. Lett. B* **89**, 253 (1980); *Phys. Lett. B* **171**, 99 (1986).
127. P.V. Landshoff, *Nucl. Phys. A* **498**, 217 (1989).
128. PHENIX Experiment at RHIC - Preliminary Conceptual Design Report, PHENIX Collaboration Report (1992).
129. E. Shuryak and L. Xiong, *Phys. Rev. Lett.* **70**, 2241 (1993); K.J. Eskola and M. Gyulassy, *Phys. Rev. C* **47**, 2239 (1993).
130. F. Wilczek, *Nuc. Phys. A* **566**, 123c (1994).
131. RHIC Letter of Intent to Study Very Low pt Phenomena at RHIC, PHOBOS Collaboration (1991).
132. Interim Design Report for the BRAHMS Experiment at RHIC, BNL Report, (1994).
133. see lectures of M. Vetterli, Proceedings of this Institute (1998).
134. The COMPASS Collaboration, CERN Proposal CERN/SPSLC 96-14 (1996).
135. C. Bourrely et al, *Nucl. Phys. B* **361**, 72 (1991).
136. C. Bourrely and J. Soffer, *Phys. Lett. B* **314**, 132 (1993).
137. R. L. Jaffe et al, MIT pre-print MIT-CTP-2672 (1997).